Trends and Perspectives in Mitigating CMAS Infiltration in Thermal Barrier Coating

Maxime Gaudin, Lucille Despres, Alice Dolmaire, Emilie Béchade, Alan Kéromnès, Simon Goutier, Alain Denoirjean, Aurélien Joulia, Vincent Rat, Armelle Vardelle

Trends and Perspectives in Mitigating CMAS Infiltration in Thermal Barrier Coating

Maxime Gaudin[1, 2], Lucille Despres[1], Alice Dolmaire[3], Emilie Béchade[1], Alan Keromnes[1], Simon Goutier[1], Alain Denoirjean[1], Aurélien Joulia[2], Vincent Rat[1], Armelle Vardelle[1]

[1] University of Limoges, CNRS, IRCER, UMR 7315, 87000, Limoges, France

[2] SAFRAN TECH, 78772 Magny les Hameaux, France

[3] DMAS, ONERA, Université Paris Saclay, F-91123 Palaiseau, France

E-mail address corresponding author (professional e-mail):

lucille.despres@unilim.fr

Abstract

The aerospace industry is facing challenges in meeting environmental and energy demands, which require a reduction in fuel consumption, emissions and production costs while improving the efficiency of aero-engines. One way to achieve this is by developing a thermal barrier coating (TBC) on the hottest components of the turbine to increase its inlet temperature. Different methods are used to deposit TBC, including air plasma spray (APS) and electron beam physical vapor deposition (EB-PVD), with each having its advantages and disadvantages. Current process developments are constantly trying to find a good compromise between intrinsic material properties, production cost and feasibility. With this in mind, suspension plasma spraying (SPS) has emerged as a viable option that can replace some applications.

However, in service, complex loadings and environmental contaminants such as calcium-magnesium-aluminosilicate (CMAS), damage the TBC and reduce its durability. After presenting the SPS process, its application to thermal barrier coatings and industrialization challenges of the process, the chapter discusses the effects of CMAS infiltration on TBC and the methodologies used to characterize the damage during engine operation. Then, it explores potential solutions to mitigate CMAS attack, including modifying the coating composition,

introducing additional layers, using SPS coatings, and developing “CMAS-superphobic” surfaces.

Chapter Keywords:

Aero engines; Thermal Barrier Coating; Suspension Plasma Spray; Yttria-partially stabilized zirconia; CMAS infiltration

Chapter outline:

1. Introduction

Climate change, caused by the release of greenhouse gases from human activities such as burning fossil fuels, is having a significant impact on the planet and is increasingly becoming a major concern for society [1], [2]. As a result, there is growing pressure on industries to reduce their greenhouse gas emissions and transition to more sustainable practices. This pressure is coming from a variety of sources, including governments, investors, consumers, and activists. Many industries, such as the power, transportation, and manufacturing sectors, are facing increasing regulations and incentives to reduce their emissions, as well as growing demand for sustainable products and services [3]. Some companies are also taking voluntary actions to address their climate impacts, such as setting emissions reduction targets and investing in renewable energy [4].

Aviation is one of the fastest-growing sources of greenhouse gas emissions. In 2021 aviation accounted for over 2% of global energy-related CO_2 emission due to the burning of fossil fuels and this percentage is projected to grow in the future as air traffic increases. The International Air Transport Association (IATA) predicts that the number of air passengers will triple by 2050, to about 8.2 billion per year [5], considering the emergence of the tourism, the demographic and economic development, especially in Asian countries. The aeronautical designers anticipate a clear high demand for passenger and cargo aircrafts (see Fig. 1). Airbus foresees 39,500 new passenger and freighter aircraft deliveries over 2022-2041 [6], while Boeing plans forecasts demand for more than 41,000 new airplanes by 2041 [7].

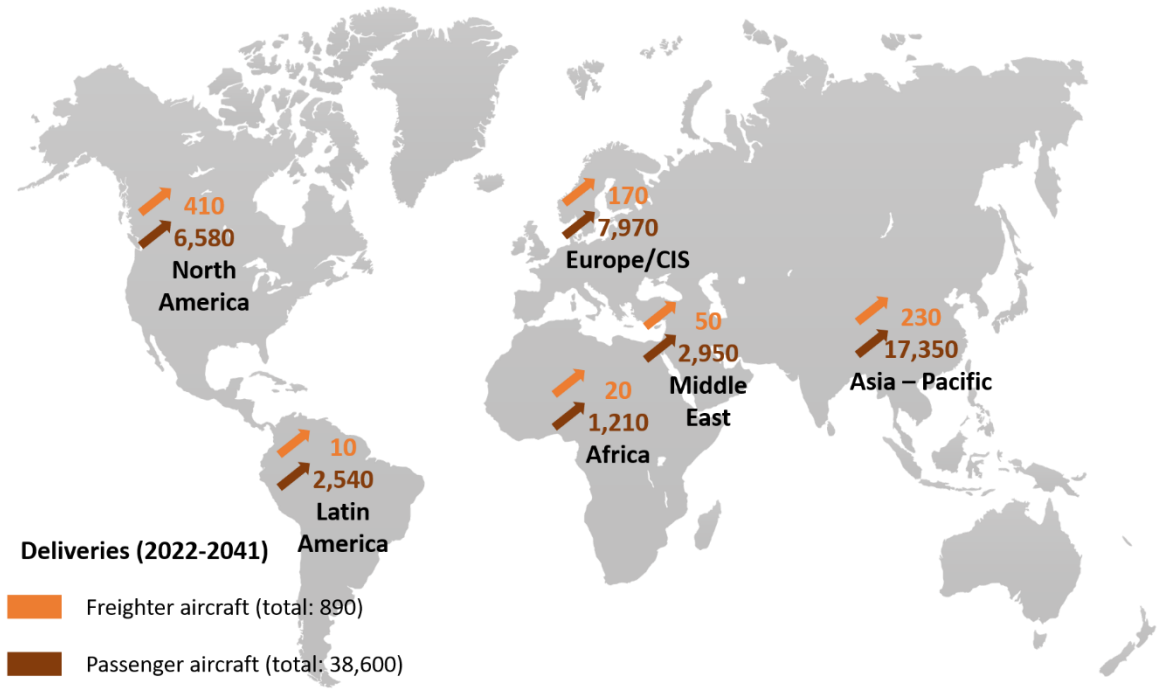

Fig. 1 Airbus freighter and passenger aircraft delivery forecasts for the period 2022-204, data collected from [6]

Additionally, the high altitudes at which aircraft fly can result in the formation of contrails, which can also contribute to warming [8]. Therefore, there is a growing interest in developing more sustainable aviation technologies and practices to reduce the environmental impact of the aerospace industry.

In 2008, leaders from across the industry came together at ATAG's (Air Transport Action Group) Aviation and Environment Summit to present a strategic vision for sustainable aviation, signing the Climate Change Action Commitment [9]. In October 2021, the global aviation industry took its climate commitment a step further by declaring that it will achieve net zero carbon emissions by 2050, supported by accelerated efficiency measures, energy transition and innovation across the aviation sector and in partnership with governments worldwide [10].

There are several ways to reduce emissions from current aircraft engines. One of them is to improve engine efficiency to generate more power while using less fuel. This is accomplished by increasing the inlet temperature of the turbines, allowing the fuel to burn at higher temperatures and pressures [11], [12]. The result is more thrust per unit of fuel consumed, resulting in a more fuel-efficient aircraft. An internal cooling network and the use of a thermal barrier coating can allow an aircraft engine's operating temperature to be increased by

effectively dissipating heat from the hottest components [13]–[15]. A commonly used thermal barrier coating for high-pressure turbine blades is a multi-layer system consisting of a bond coat, a thermally-grown oxide and a ceramic topcoat that are deposited on a single crystal nickel-based superalloy [15], [16]. The bond coat bonds the other layers to the substrate and protects it from oxidation by forming a stable, slow-growing, adherent alumina layer. The top coat provides insulation to protect the blade from the high temperatures encountered during operation. It is usually made of yttria-partially stabilized zirconia (ZrO_2-6 at 8% wt. Y_2O_3). This material was chosen because of its high coefficient of expansion for a ceramic, its low thermal conductivity, its high toughness, its structural stability at high temperatures, its chemical stability against the oxidizing environment of fuel gases, its compatibility with the underlying alumina layer and its compatibility with a deposition process. Its intrinsic properties are largely controlled by its microstructure, which depends on the deposition process.

Currently, two deposition techniques are commonly used to deposit the ceramic topcoat [17]. In systems with low mechanical stress as engine's combustion chambers, it is deposited by atmospheric plasma spraying (APS). The coating has a lamellar microstructure that reduces its thermal conductivity. For more stressed systems, such as aeronautical turbine blades, the topcoat is deposited by evaporation (EB-PVD: Electron Beam Physical Vapor Deposition) and has a columnar structure, which is advantageous for mechanical properties (better strain tolerance and thermal shock resistance) but detrimental for thermal properties. In addition, EB-PVD has several other drawbacks: high cost, complexity of operation and maintenance, low deposition rate, high-energy consumption and limitation of deposition to small areas [16].

Today, coating processes based on the simpler principle of APS are being developed; they aim to replicate in some way the microstructure of EB-PVD coatings but with lower thermal conductivity [11], [17]–[20]. They include plasma spray physical vapor deposition (PS-PVD), solution precursor plasma spray (SPPS), and suspension plasma spray (SPS). It is expected that they will be used for both the combustion chamber and the high-pressure turbine components. Suspension plasma spray process is now emerging at an industrial level and will be the focus of this chapter.

In service, high-pressure turbine blades are subjected to damage mechanisms that are classified into intrinsic and extrinsic mechanisms [21]. The latter are related to particle ingestion and severe environment and will be described in detail in section 2 of this chapter.

The intrinsic mechanisms are induced by the differences in thermomechanical properties of the different layers of the system. Indeed, the operation of the engine at high temperature (1200°C) leads to the dissociation of the metastable phase of the yttria- partially stabilized zirconia (noted "YSZ" in the chapter) into a cubic phase, richer in yttrium, and a quadratic phase, poorer in yttria, which is likely to be transformed into a monoclinic phase (<200°C) during the cooling of the engine [22]. These phase changes induce localized volumetric variations of the thermal barrier, creating residual stresses, which can lead to delamination of the TBC [23]. In addition, TBC is subject to thermal aging. Repeated flight cycles above 1200°C lead to its sintering, i.e., densification of the thermal barrier, which induces additional residual stresses during engine cooling and reduces the thermal insulation capacity of the TBC. Finally, the thermomechanical fatigue at high temperature (>1100°C) leads to an evolution of the interface between the under-layer and the ceramic. This evolution depends on the morphology and the nature of the bonding layer, but also on the thermal conditions surrounding the system (isothermal or not). This interface zone, called TGO (Thermally Grown Oxide), is an alumina (α-Al_2O_3) oxide, which is necessary to limit the corrosion phenomena. However, the progressive oxidation of the bonding layer will increase the thickness of this layer during engine thermal cycles and induces high residual compressive stresses during cooling (3 to 6 GPa at room temperature [24]. The stress relaxation then deforms the surface of the TGO ("rumpling" or "ratcheting" phenomenon), causes localized separation zones at the TGO/ceramic interface and promotes the nucleation of cracks [21], [24]. These defects grow as the thermal cycles are repeated, until they cause spalling of the TBC.

The increase in temperature inside the engine leads to additional extrinsic damage mechanisms as dust, sand, and volcanic ash, commonly referred to as calcium-magnesium-alumino-silicates (CMAS), which are ingested by aircraft engines, melt at a temperature close to 1240°C [24] and infiltrate the top coat. This infiltration leads to chemical reactions with the partially yttria-stabilized zirconia and induced mechanical stresses during engine cooling, which can be very detrimental to the lifespan of the thermal barrier coating system [21]. Therefore, new thermal barrier coating systems need to prove their thermomechanical performance and durability in a harsh environment where they can be subjected to the CMAS problem.

This chapter mainly addresses this issue and focuses on CMAS infiltration mitigation strategies using suspension plasma spray (SPS) coatings. It first describes the SPS process and its current challenges, keeping in mind an objective view of economic, industrial, and technological

realities. It then describes the thermomechanical degradation and chemical reaction between the TBC and molten CMAS. Next, it presents some methodologies used to evaluate the behavior of thermal barrier coating systems during engine operation and their resistance to CMAS attack. Finally, it presents the current potential solutions against CMAS attack including the use of SPS coatings. The conclusion provides some perspectives on potential solutions.

2. Suspension Plasma Spray

2.1. Process description

Thermal spraying belongs to the family of dry deposition techniques and refers to ballistic processes. It consists in accelerating and spraying solid particles on a prepared surface to form a coating resulting from the accumulation of flattened particles (splats). The deposition mechanism is based on the deformation of particles at impact and it can be achieved at low temperature only for metallic particles due to their plastic deformation [25]. However, in the case of micron-sized ceramic particles and owing to their brittle property, they have to be in molten or semi-molten state to form splats upon impact. A thermal plasma jet, generated by a non-transferred arc plasma torch, is usually used as a relevant heat and momentum source for high-melting point materials like ceramics [26].

A plasma forming gas mixture (e.g. Ar, H_2, N_2 or He) is injected into the torch body while an electric arc is generated between the electrodes with a particular design including the inter-electrode space, the gas injection ring and eventual neutrode stack arrangement [27]. Plasma jet's core temperatures at the nozzle exit can reach up to 13,000 K [28], [29]. The velocities of the plasma jet are between 900 and 2000 $m \cdot s^{-1}$ depending on plasma conditions, torch design and electrical power [30]. In Atmospheric Plasma Spraying (APS), the powders, processed at atmospheric pressure, have diameters generally between approximately 5 and 50 μm. They enter the plasma core and move with a velocity on the order of 150 to 300 $m \cdot s^{-1}$ [31]–[33], resulting in the formation of lamellar coatings with a porosity on the order of 5 to 20% [31].

At the beginning of the 2000s, the needs of new generation thermal barrier coatings used in harsher environment, prompted research into improving the thermal insulation and

thermomechanical performance of TBCs. This has led to the development of thermal spray processes that take advantage of nanometer and submicron materials [34]–[36].

The submicron-sized particles must have enough momentum to penetrate the plasma jet. The technological choice was therefore to trap them in a liquid phase to efficiently inject them in the plasma core. This injection method has highlighted some major issues related to plasma interactions with the liquid phase and to the subsequent particles' treatment. The liquid phase is composed of submicron particles dispersed by means of chemical additives within an aqueous or alcoholic solvent forming a suspension. The key properties of the suspension, such as density, viscosity, surface tension, vaporization latent heat of the liquid depend on particle size distribution, solvent, and powder loading rate. The suspension properties associated with the injection direction (axially or radially to the plasma jet) have a predominant influence on the deposit microstructure due to plasma/suspension interactions [37], [38].

Suspension plasma spraying (SPS) process has succeeded in attracting the interest of researchers and manufacturers due to the easy obtention of a relatively large range of microstructures. SPS has become a competitive deposition process of thermal barrier coatings not only in terms of improvement of coating properties but also in terms of cost-effectiveness [16], compared to the EB-PVD process. However, plasma-related process parameters must be considered and require specific optimization for each type of desired microstructure.

2.2. Process parameters influencing the coating formation

Empirical models obtained from the observations of the first layers of SPS coatings suggest that particle size, direction and impact velocity have a dominant influence on the resulting coating morphology [19], [39]–[45]. The surface preparation of substrates is also a significant parameter, especially the surface roughness (mainly Ra and Rsm) [40], [46], [47]. The size of impacting particles and their directions upon impact combined with the surface roughness lead to a "shadow effect", particularly accentuated by the smallest particles [41]. Indeed, for low Stokes numbers (<1), particles tend to follow the streamlines of the plasma flow which means that their velocity component parallel to the substrate surface is increased. Larger particles, less subjected to plasma jet streamlines, form large splats onto the substrate surface, giving rise to more homogenous and larger columns and/or homogeneous lamellar structures. A critical impact velocity between 50 and 70 $m \cdot s^{-1}$ is required to ensure particle spreading of a YSZ

suspension of median diameter 0.7 μm [48], [49]. Below this critical velocity, fine particles do not spread on the target surface, even when the target is preheated to high temperatures (approximately 500°C). These particles with low Stokes numbers and low impact velocities form stacking defects (porosities, encapsulated particles, …) in the coating microstructure, promoting columnar structures.

The formation of SPS coatings and their microstructures depend on the heat and momentum transfers from plasma species to particles that govern their trajectories in the plasma jet. Submicron and nanometric-sized particles will be more strongly subjected to the lesser hydrodynamic fluctuations of the plasma flow [50] and to all velocity and temperature gradients encountered during their flight [51], [52], [53].

Three main categories of first-order operating parameters are important to control: 1) suspension properties and injection method, 2) plasma torch parameters (torch design, arc current, electrical power, plasma forming gases, their mass flow rates), 3) bench conditions (spraying distance, scan velocity, substrate surface condition) [19], [39], [45], [53]–[57].

The torch parameters should be optimized according to the suspension properties to promote the suspension fragmentation and solvent evaporation into the plasma jet [37]. A high electrical power of the torch and a high total mass flow rate of the plasma forming gases promote respectively the degree of solvent evaporation and particle melting on the one hand, and the efficiency of fragmentation and the low residence time of particles in the plasma on the other hand [54]. The average plasma specific enthalpy and the average plasma velocity are the derived physical properties from these torch parameters. They can be used as generalized measures to study the evolution of coating morphologies. For instance, a study showed the impact of these measures on the width and densification controls of columns in SPS coatings [53]. The hydrogen content of the plasma forming gases specifically increases the plasma enthalpy significantly and leads to better heat transfers. It turns out that a balance must be struck between fragmentation/evaporation efficiency that provide small particle size distributions and the need to generate particle streams with high Stokes number to achieve higher deposition rate efficiency and fewer stacking defects (fewer particles flowing around the target or not sticking to the surface).

The spraying distance and the scanning speed respectively modify the residence time of the particles and the stacking area of the splats on the target. In fact, these two easily controllable

parameters have a significant effect on the direction and velocity gradients of the plasma jet as well as on the coating morphology [59]–[63].

A wide variety of coating morphologies is thus possible to achieve due to the sensitivity of the fine particles to each process parameter, resulting in coatings that are more or less dense, comprising of narrow to flared columns or forming a more homogeneous lamellar layer [55], [64], [65]. The versatility of the microstructures (see Fig. 2) that can be obtained by the SPS process is one of its main advantages, compared to the APS process.

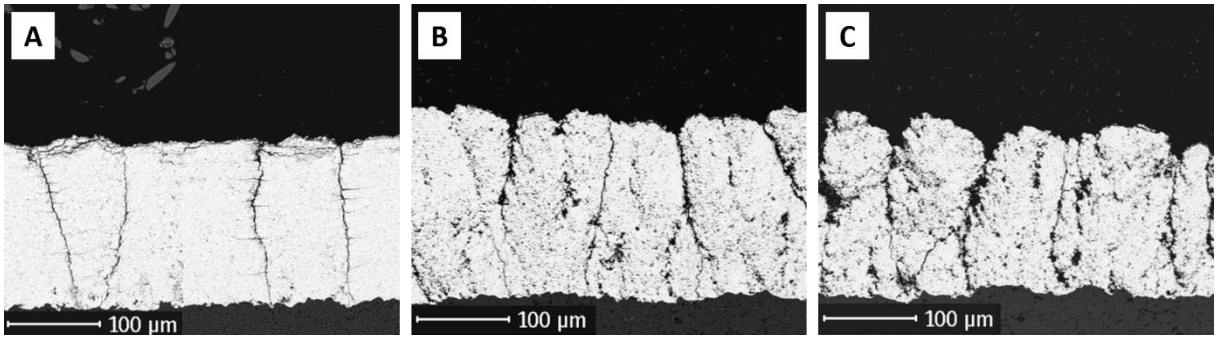

Fig. 2 Examples of microstructures obtained by Suspension Plasma Spraying: A dense vertically craked (DVC), B compact columnar and C columnar microstructures

2.3. Challenges of SPS coatings: the case of high-turbine blade TBCs

Due to the specific columnar microstructures provided by SPS, several comparative studies have shown that, in isothermal thermo-cyclic fatigue tests at 1100°C, SPS TBCs have a longer lifetime than APS coatings (up to 450 cycles for SPS coatings versus 300 for APS coatings for instance) [66], [67]. There are three major reasons for this difference:

- The internal porosity of the coating that relaxes thermomechanical stresses at the interface with the thermally grown oxide (TGO), one of the main places of damaging with this test (further details in section 4).
- The roughness state of the bondcoat surface which affects the crack propagation energy in the coating [68].
- The oxidation rate of the bondcoat depending on its chemical nature which will then affect the state of stress at the TGO-coating interface.

In these comparative studies, measured porosity levels and the columnar microstructure generated by the SPS process allow to relax more efficiently the thermomechanical stresses at the interface with the TGO, which is a targeted feature for high-turbine blades TBCs.

The erosion resistance of SPS coatings can also be improved to APS and EB-PVD coatings [69], [70]. Crack propagation caused by projectile impacts is limited by the column width in the case of columnar SPS coatings compared to APS lamellar coatings where cracks propagate more easily between the lamellae as hypothesized by Mahade et al [69]. The depth of erosion within these lamellar coatings also gets higher with the same amount of erosive projectiles, meaning more coating material is delaminated compared to SPS coatings [69].

Another technical advantage of SPS columnar deposits is their low thermal conductivity. Indeed, it has been shown that SPS coating morphology (porosity, column widths and inter-column spaces) influences the type of thermal diffusivity mechanisms in yttria-stabilized zirconia coatings [55], [64], [71]. In the case of a coating with "compact" columns (very narrow inter-columnar spaces to none), there are no possible direct air conducts down to the metallic substrate and therefore no contribution of radiation in the thermal diffusivity [46], [71]. Heat diffusion in this coating is significantly reduced compared to coatings with more spread out columns (diffusivity of $3.0 \cdot 10^{-7}$ $m^2 \cdot s^{-1}$ versus $6.0 \cdot 10^{-7}$ $m^2 \cdot s^{-1}$ for the most “open” structure) and is close to the dense APS coatings (diffusivity of $3.5 \cdot 10^{-7}$ $m^2 \cdot s^{-1}$). Some of the columnar coatings tested in these studies also exhibit lower thermal conductivity than the EB-PVD coatings currently used on turbine blades [64]. These results can be explained by the presence of more tortuous air conducts or even the absence of such conducts in columnar coatings produced by SPS compared to the numerous straight air conducts between the columns of EB-PVD coatings. The tortuosity and width of these conducts can be controlled by changing only the scanning velocity of the torch in front of the substrate, according to Bernard et al. [19], [71]

The greater thermal insulation of SPS coatings compared to EB-PVD coatings may also be related to the multi-scale nature of the porosity of SPS coatings (micro-, submicro- and nano-porosity). This multiscale porosity makes thermal conduction pathways more difficult within the coating material compared to EB-PVD coatings with dense columns. All of this data and assumptions are summarized in Fig. 3.

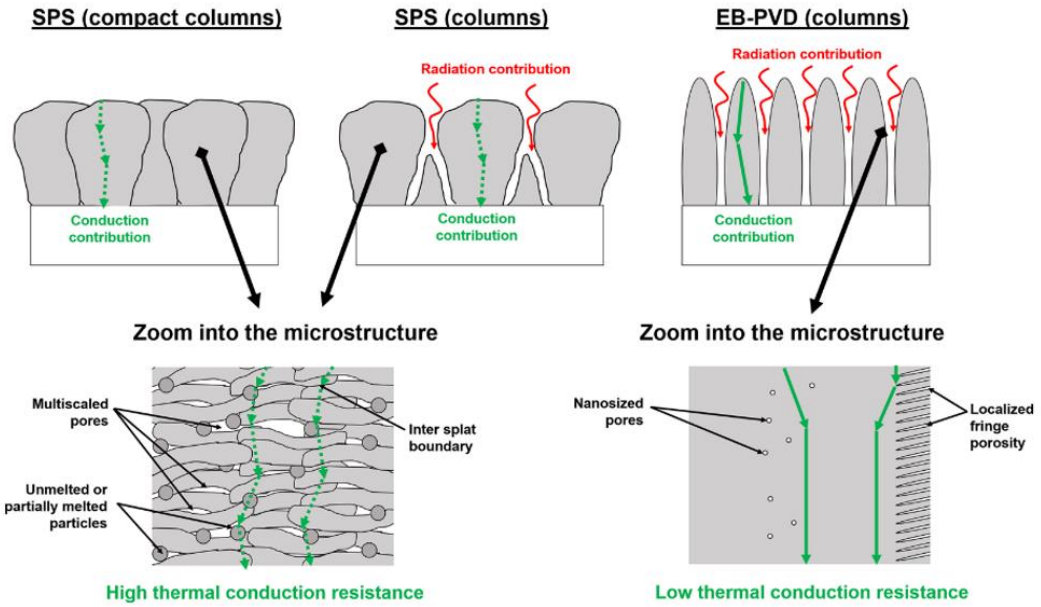

Fig. 3 Summary of thermal conduction paths in coatings for different deposition methods [46]

Lower thermal conductivity values were also found when comparing several SPS conditions leading to different YSZ coating morphologies compared to a dense, vertically cracked APS-sprayed YSZ coating (thermal conductivities between 0.8 and 1 $W \cdot m^{-1} \cdot K^{-1}$ at 25°C for SPS coatings versus 2 $W \cdot m^{-1} \cdot K^{-1}$ for APS coating) [67], [72]. All these studies show the advantage of the multi-scale porosity obtained by the SPS process compared to coatings from currently used technologies presenting a less varied porosity.

Nevertheless, the industrialization of this process is still encountering some "lock" regarding the reproducibility of the coating morphology and thickness along complex surfaces such as high-turbine blades. The morphology of the coating can vary with the curves, hollows and hills of the blades (see Fig. 4) [40], [46], [49]. In-depth knowledge is currently necessary to better assess particles' dynamics at impact upon these complex surfaces and to find ways to mitigate effectively these morphological differences.

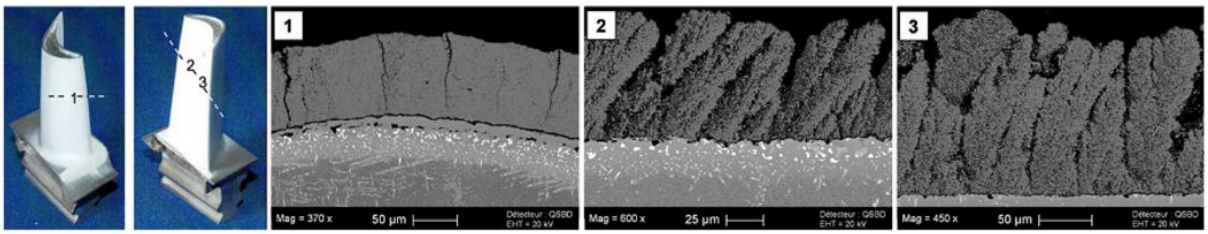

Fig. 4 Photograph of a coated high-pressure turbine blade covered after SPS (far left) and then micrographs of the obtained coating morphologies obtained as a function of the covered surface [46]

The evolution of the thermal and chemical environment applied to TBCs must also be taken into account during the development of these coating processes. Indeed, as the operating temperatures of aeronautical turbines increase, thermal barrier coatings are facing more severe and increasingly corrosive environments. Three types of hot corrosion encountered can be listed:

- corrosion initiated by sodium sulfates (Na_2SO_4) formed during fuel combustion and by sulfur in the fuel
- The double thermochemical and thermomechanical attack of silicate particles, named CMAS (for CaO, MgO, Al_2O_3, SiO_2-rich particles), which are ingested by the engine during all phases of use. These particles are usually sand or volcanic ashes.
- Corrosion initiated by the combustion of so-called sustainable aviation fuels (SAF) developed by the aviation industry to reduce their fuel consumption. [73]–[75].

The degradation mechanisms related to CMAS environment seem to be predominant for the new generations of TBCs and their complexity requires further explanations, given in the following sections, keeping in mind the development of SPS coatings.

3. Damage mechanisms of CMAS infiltration

The air ingested by aircraft engines contains various siliceous particles (CMAS), the nature and size of which depend on their geological origins and the regions of the world over which the aircraft fly (desert, volcano, urban environment, ocean...) [76]. These airborne particles are being studied by various laboratories around the world, not for their direct effect on TBCs, but on human health [77]–[79]. In the Earth's atmosphere, the concentration of small diameter particles (≤2.5 µm: $PM_{2.5}$) is naturally relatively low: between 5 and 35 $\mu g \cdot m^{-3}$ [80], [81]. However, in highly urbanized or industrialized areas such as airports, this value can increase up to 10-fold [81], [82]. Aviation safety authorities have set the maximum particulate matter threshold for air travel, at 2 $mg.m^{-3}$. Particle concentration reach maximum values during volcanic eruptions or sandstorms. Therefore, desert regions and areas close to volcanoes are the places with the highest concentrations. In the deserts regions of Iran, for example, the concentration of PM_{10} particles (diameter less than 10 µm) reaches an average of 5479 $\mu g \cdot m^{-3}$ on sandstorm days, [83], [84], whereas during routine days (without sandstorms) the daily PM_{10}

concentration averages less than 200 $\mu g \cdot m^{-3}$ in most desert regions [85]–[90]. In 2010, during the eruption of the Icelandic volcano Eyjafjallajokull, the PM_{10} concentration reached a maximum value of 13,000 $\mu g \cdot m^{-3}$. As a result of this eruption, air travel had to be suspended (108,000 flights cancelled [91]), resulting in an estimated loss of between US$ 1.7 and US$ 3.3 billion to the aviation industry [92]–[94].

Take-off, landing and cruise periods, are all phases when particles are likely to enter aircraft engines. The airflow ingested by the engine guides these particles to the high-pressure turbine blades where the thermal environment is severe (>1600°C). However, only a portion of the particles in the secondary air stream are deposited on the blades and initiate a chemical and mechanical reaction on them. Several models have shown that, depending on the generalized values of the Stokes number, a particle tends to follow the airflow or to deposit on the surface of the blade [95]–[98]. This Stokes number depends on the morphology and chemical composition of the particle, as well as the characteristics of the air flow (namely velocity and dynamic viscosity) [99]. The higher the generalized Stokes number is, the greater is the probability of a particle impacting a turbine blade.

It has been shown that it is primarily particles between 4 and 10 μm in diameter that are deposited on the turbine blades [80], [97], [100], [101]. The next sections are going to focus solely on CMAS infiltration within TBCs and the damage mechanisms therein, letting aside other aspects of CMAS attack on TBCs such as erosion or clogging effects into the leading airducts.

3.1. Chemical mechanisms of CMAS infiltration attack

Silica (SiO_2) is the main component of CMAS particles, seconded by lime (CaO). Depending on the content of complementary oxides contained in these CMAS particles contain (MgO, Al_2O_3, Fe_2O_3, TiO_2, etc.), the thermochemistry of the particle changes. In particular, the melting point of silica (1730°C) is strongly impacted by these chemical variations. In flight in such hot environments, CMAS particles present a significant risk of glass formation, whose reactivity with TBC is conditioned by various interdependent physico-chemical characteristics of CMAS, such as: particle size, basicity index, glass transition point T_g, and rheological properties (viscosity, wettability).

Table 1 below classifies the main oxides constituting CMAS according to their thermochemical characteristics [102]–[104] and their modes of action on the formation of a glassy network [105].

Table 1 Thermochemical characteristics of the various oxides involved in the composition of glassy networks

		Metal oxidation state	Coordination Number CN	% ionicity (Stanworth's criterion)	Cationic radius	Melting point T_F	Bond Strengh F_{M-O}	Cation field Strenght FS^1	Rawson's criterion F_{M-O}/T_F
					(Å)	(K)	(kcal.mol^{-1})	(Å^{-2})	(kcal.mol$^{-1.}$ K^{-1})
Acidic oxides / Lattice formater	**SiO_2**	4	4	51	0,4	1993	106	1,23	0,053
	P_2O_5	5	4	39	0,38	843	88-117	1,58	0,104-0,131
Basic Oxide/ Lattice modifier	**CaO**	2	8	79	1	2773	32	0,35	0,011
	MgO	2	6	73	0,72	2913	37	0,44	0,013
	Na_2O	1	6	82	1,02	1132	20	0,17	0,018
	K_2O	1	9	84	1,38	646	13	0,13	0,02
Amphoteric oxides / Intermediate oxides	**Al_2O_3**	3	4	63	0,39	2072	101-79	0,94	0,038-0,049
			6		0,54		53-67	0,8	0,032-0,026
	ZrO_2	4	7-8	67	0,8	2923	81	0,83	0,023

[1]The cation field strength is defined as $FS = Z/(Rc+Ra)^2$, where Z is the charge, Rc and Ra are the radius of cation and anion, respectively, with the appropriate coordination number (CN).

The addition of lattice modifying oxides, mainly composed of alkali or alkaline-earth oxides (such as CaO, MgO, …), has the effect of depolymerizing the glass lattice by breaking the bridges of the forming oxide, Si-O-Si in the case of CMAS. The alkali or alkaline-earth cation is positioned in close proximity to one or two "non-bridging" oxygens created, to ensure electrical neutrality. The ionic field strengths (FS ~ 0.13 – 0.44 $Å^{-2}$) are weak because of the small size and charge of the cations. They become highly mobile in the CMAS glass, but also ultimately have a strong polarizing effect on the chemical bonds at the interface with the TBC.

The basicity index (BI) of CMAS (Eq. 1), is used to classify CMAS into three categories, according to their formulation [106]–[109]:

$$\text{BI } (Basicity\ Index) = \frac{\sum Basic\ oxides\ (mol.\%)}{\sum Acidic\ oxides\ (mol.\%)} \qquad (\text{Eq. } 1)$$

Intermediate oxides such as Al_2O_3, TiO_2, or ZrO_2 participate in the BI equilibrium in two ways:

- If they act as nucleating agents (for low BIs), they result in promoting the germination/growth of microcrystals within the glass (e.g. anorthite formation),
- If they act as a stabilizing agent of the glass network (high basicity index >2.2), they are found in high concentrations in the melt (as amorphous phases) *via* the introduction of new eutectics [103].

The composition of CMAS particles is a variable data and strongly depends on the geographical factor. Fig. 5 compares different compositions of natural and artificial CMAS.

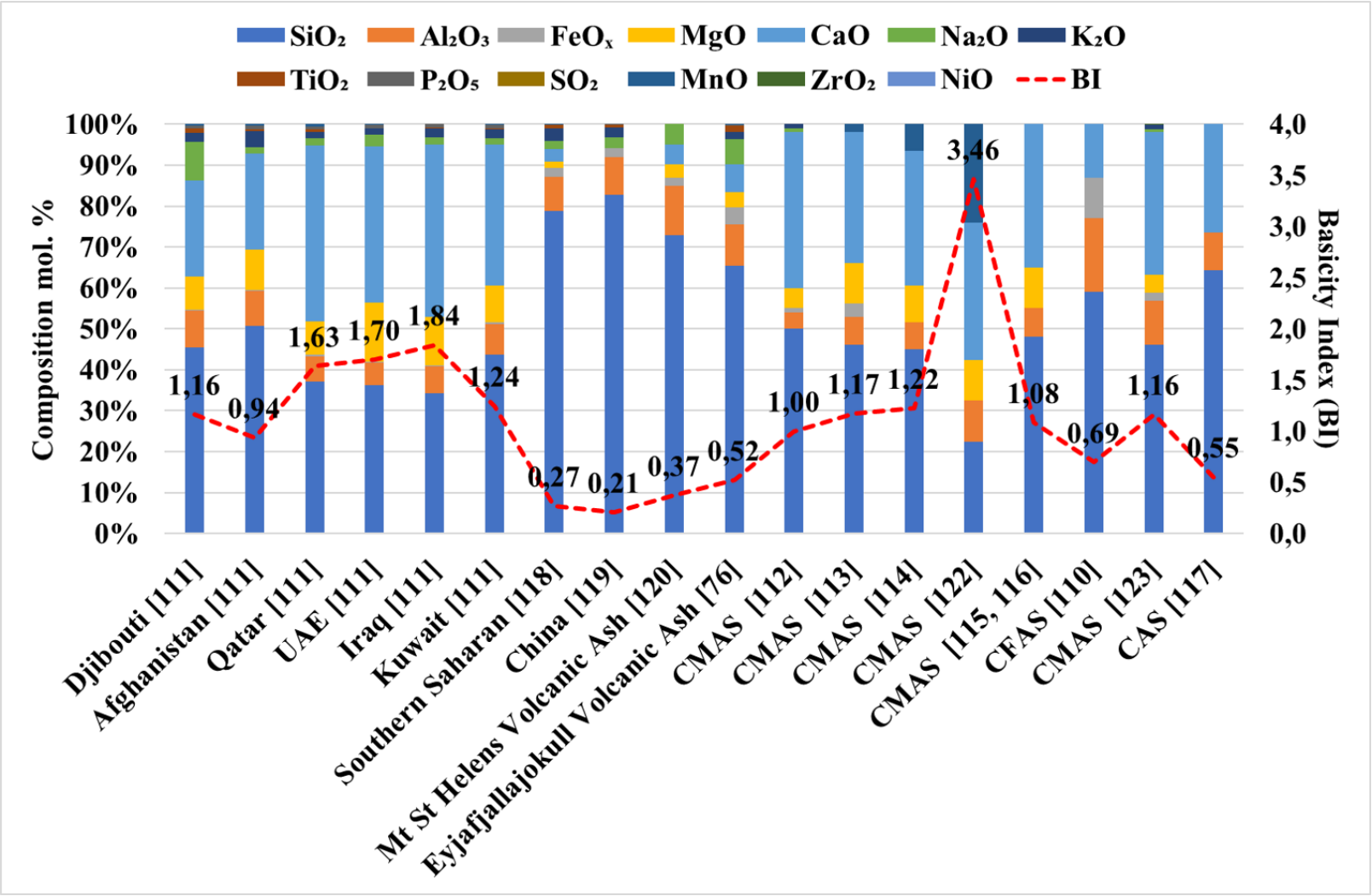

Fig. 5 Composition of different CMAS used in the laboratory and naturally occurring particles (PM_{10}) in different regions of the world - with basicity index for each composition, data collected from [76], [110]–[123]

The majority of CMAS studied in the literature have a basicity index below 2.2 [103], [124] (Fig. 5) and glass transition temperatures below 1300°C. Upon slow cooling, they can therefore form relatively stable crystalline phases, in the polymorph range of $CaSiO_3$ pseudo-wollastine and anorthite $(Ca,Mg)Al_2Si_2O_8$ for CAS and diopside $CaMgSi_2O_6$ or merwinite $Ca_3\ Mg(SiO_4)_2$ mixed with akermanite $Ca_2MgSi_2O_7$ in CMAS depending on the CaO/SiO ratio [112], [113], [125]. For high basicity index (BI>2.2), the addition of lime, normally used in small amounts to increase the chemical resistance and decrease the solubility of the glass, conversely causes devitrification and an increase in the melting temperature of the mixture formed [126], [127]. The intermediate oxides act as network-forming agents to compensate for this effect. The precipitated and crystallized phases must then contain a significant amount of calcium in their structure. The $CaO\text{-}AlO_3\text{-}SiO_2$ ternary phase diagrams give a very complete description of these equilibria. The implementation of these databases, for more complex systems, combined with thermal and XRD analyses, gives a complete description and characterization of the phase equilibria and liquidus layers (viscosity calculation) for multiple CMAS [128]–[130].

Chemical degradations caused by sands from different regions of the world or over different service times have thus resulted in a large number of studies that show a relatively similar degradation mechanism for the most widely used YSZ TBCs [113], [114], [131]–[134]. CMAS particles (less than 30 μm in diameter [135], [136]), which enter the hot section of the aircraft engine, undergo a rapid change of state and become molten, due to the very high temperatures in the combustion chamber (1400-1800°C) as well as in the turbine inlet (around 1600°C). This now viscous CMAS, totally or partially transformed in the combustor, sticks to the surface of the TBCs on which the temperature of the CMAS can quickly reach the glass transition point. There, the melt steeps into the inter-columnar spaces or into open porosities of the TBC. At the $(liquid)_{CMAS}$ / $(YSZ)_{TBC}$ interface, new amorphous or crystalline oxides precipitate by thermochemical exchanges [113], [117], [126], [128], [129], [131], [137].

The infiltration of molten particles is facilitated by their low viscosity and good wettability towards the zirconia lattice [114], [138]. Y^{3+} cations (FS ~ 0,46 $Å^{-2}$, close to the well-known modifier Mg^{2+}) diffuse progressively into the infiltrated glassy phase, and act on the non-bridging oxygens of the glassy lattice. Zr^{4+} cations also diffuse into the glass and act as nucleating agents similar to Al^{3+} due to their similar field strength (FS ~ 0.62 $Å^{-2}$). They form precipitates such as $Ca_2Zr(Y)Si_4O_{12}$, for low or mid-range BI (< 2) [114], [117]. These diffusion mechanisms lead in parallel to the formation/re-precipitation of nanometric zirconia nodules at the $(liquid)_{CMAS}$ / $(YSZ)_{TBC}$ interface (see Figure 6), weakly stabilized in yttria Y_2O_3 (t phase)

[21], [117], [137], [139]. These globular particles or nodules are not stable, creating potentially mechanically brittle areas over the temperature changes, due to the polymorphic nature of zirconia over the operating temperature range of aircraft engines [23], [64], [113], [126], [140], [141]. For high BI (>2.2), the high concentration of lime results in favored precipitation of various cubic calcium zirconates (such as $CaZrO_3$) [103]. The proportion of acidic cations (Si^{4+}, Al^{3+}) is low, or non-existent, in these precipitated areas ensuring the cross-linking of the infiltrated glass. All these thermochemical damages lead to a very fast degradation and infiltration (<1min at 1240°C in EB-PVD coatings) of the TBC [114]. Only the nature of the reprecipitated phases varies depending on the role that the intermediate oxides take, i.e., depending on the basicity index of the melt [113], [115], [126], [142]–[144].

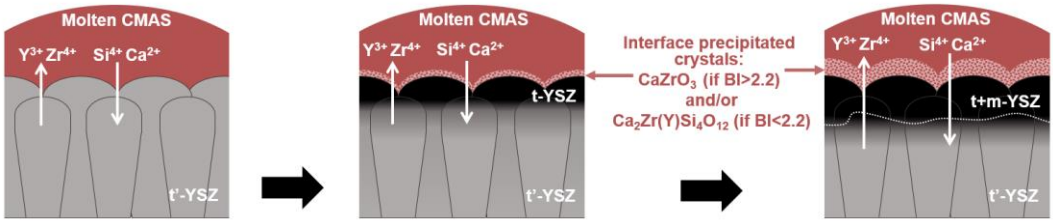

Fig. 6 Schematic of the dissolution-precipitation mechanism leading to the destabilization of YSZ upon contact with glass melt. Upon exposure to the CMAS molten the tetragonal phase dissolves more rapidly. The chemical potential gradients between the layers lead to the formation of an intermediate phase enriched in Ca, Zr, Y, Si (such as $CaZrO_3$ or $Ca_2Zr(Y)Si_4O_{12}$ phases). Below this zone, the Y-depleted zirconia phases precipitate epitaxially (black area) forming a shell on the remaining undissolved YSZ core (grey area). The shell transforms into a monoclinic phase upon cooling, and the ensuing stresses trigger transformation of the marginally stabilized core.

The degree of intensity of CMAS melt attack on the TBC also increases with the concentration ([CMAS]) and exposure time (Δt) of CMAS particles inside the aircraft engine [145], [146]. To characterize this intensity, the "particle dose" was introduced by Clarkson et al. as follows (Eq. 2):

$$\delta = [\mathrm{CMAS}] \times \Delta t \qquad \text{(Eq.2)}$$

Using this tool, they were able to generate a diagram predicting the damages ensured by a Rolls Royce aircraft engine as a function of exposure time and airborne concentration of different types of CMAS [147], [148] (Fig. 7).

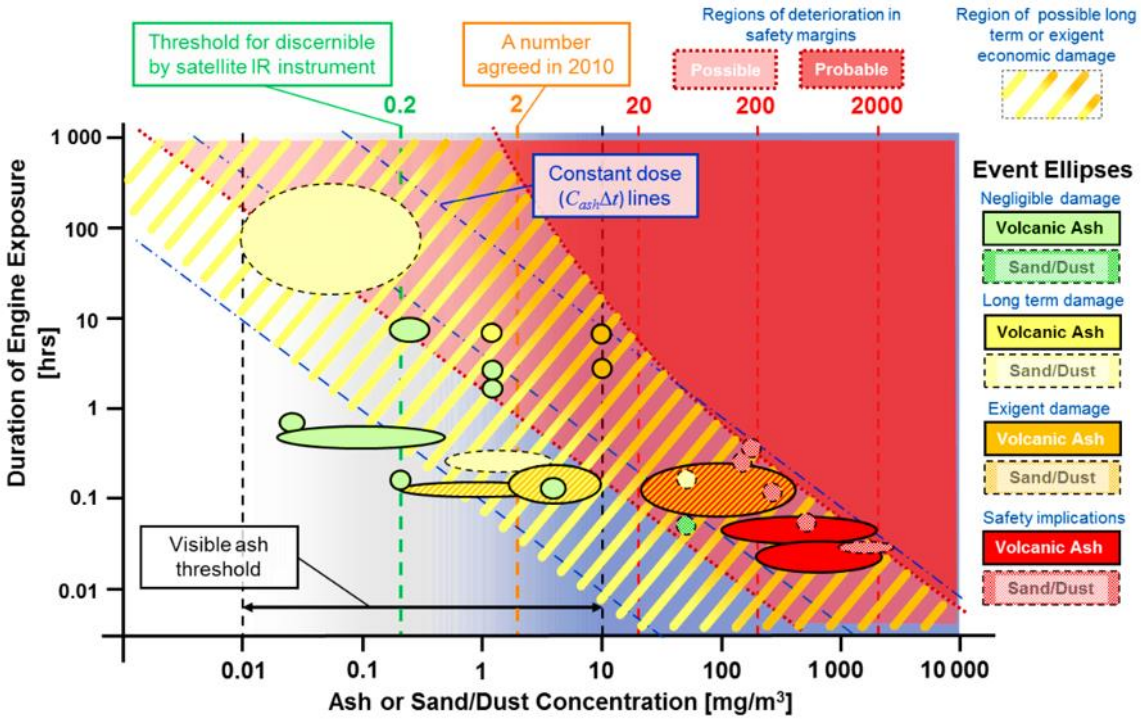

Fig. 7 Diagram illustrating the duration of exposure of an engine to a concentration of particles (sand or ash), indicating safe areas of use [147]

3.2. Mechanical damages induced by CMAS infiltration attack

Molten particle infiltration (CMAS) not only causes thermochemical degradations but also generates significant mechanical stresses in the topcoat, leading to its spalling. These stresses are dependent on the microstructure of the coating and evolve with the thickness of the coating, which is probably due to the thermal gradient experienced in service [133], [140].

In the case of a dense lamellar microstructure, it appears that CMAS particles infiltrate into pre-existing cracks and pores in the thermal barrier coating due to capillary forces that cause the separation of the inter- or intrasplat boundaries, resulting in expansion of the coating volume. This expansion induces compressive stresses due to the physical constraint of the substrate on the top coat, which can lead to buckling to release the stress. This buckling process occurs at elevated temperatures. As the CMAS gradually solidifies during the cooling process, it sets the buckling shape, but the thermal expansion coefficient mismatch between the metallic part, the

corroded topcoat and the non-penetrated topcoat can still cause an increase in bending [132], [149]–[151].

In the case of a columnar coating, it appears that during cooling, solidification of the infiltrated CMAS stiffens the topcoat (higher Young's modulus) and reduces its ability to resist accommodative deformation. Rapid cooling appears to initiate high in-plane tensile stresses in the topcoat, leading to the opening of vertical cracks from the top surface downward in the thermal barrier coating. In addition, stress accumulation, probably due to thermal expansion coefficient mismatch, promotes horizontal cracking in three main areas: just below the top surface of the topcoat, at the interface between the CMAS-penetrated and non-penetrated areas, and near the topcoat/bondcoat interfaces [152]. The various authors working on the subject seem to agree on the delamination mechanisms but not necessarily on the nature of the stresses induced during the cooling phases [140], [151], [152].

It is, therefore, necessary to provide additional answers on the mechanical stresses induced by the infiltration and solidification of these molten particles, especially as they seem to depend on the microstructure of the coating. It appears that these stresses are the main factor leading to the spalling of thermal barrier coatings. This type of degradation affects all types of TBC, regardless of the microstructure or the deposition process [113], [140], [141], [153].

In summary, the intensity and mechanisms of CMAS infiltration in TBCs vary depending on the following parameters:

- The amount of CMAS particles deposited on the TBC surface. It is proportional, at constant temperature, to the concentration of CMAS particles in the air and to time. It is directly related to the Stokes number of CMAS particles in the aircraft engine.
- Temperature at the surface of the TBC. It determines the melting state of the deposited CMAS particles. As a result, CMAS melts exhibit changing viscosity and surface tension, increasing or decreasing contact on the TBC and the degree of the chemical attack intensity.
- The quantity and size of open porosities, cracks, inter-columnar spaces… on the TBC surface. They influence the number of entry points for molten CMAS into the coating and the volume of interaction with the TBC [105], [154].
- The chemical composition of the molten CMAS. It influences the infiltration rate of molten CMAS into the TBC as well as the nature of the phases formed at this interface with respect to thermochemical reactivities and kinetics [103], [124], [155].

- Engine temperature cycles. They cause repeated thermal shocks and vitrification upon cooling of CMAS infiltrated into TBCs, leading to the accumulation of residual stresses and eventual delamination of the attacked TBC.

Since CMAS-induced degradation of thermal barrier coatings is a complex phenomenon, it is crucial to consider the multifactorial nature of these effects when testing the durability of TBCs. To do so, the characterization method employed must be both appropriate and rigorously controlled to provide the most accurate diagnosis possible.

4. Methodologies for characterizing damage to SPS coatings, including CMAS

It is essential to consider the environment surrounding the aircraft engine parts during the heating and cooling cycles as accurately as possible if the durability of TBC under CMAS attack is to be realistically characterized. In the case of high-pressure turbine blades, the surface of the TBC is naturally coated with molten CMAS particles less than 30 µm in diameter and is exposed to temperatures typically above 1200°C in a corrosive atmosphere. The underlying metal turbine blade has multiple air-cooling channels leading to the TBC surface. These opening channels also allow the formation of an air film on the TBC surface that simultaneously reduces its surface temperature. At the end of the engine thermal cycle, a sharp temperature drop is observed within 3 to 4 minutes. Thus, in order to evaluate the thermal barrier resistance to the environment in which it evolves, the means of characterization must be able to simulate as well as possible these thermal, mechanical and chemical constraints.

Two main tests are currently used to characterize the durability of TBCs at high temperature: the isothermal cycling test and the thermal gradient cycling test. In both cases, the durability of TBCs is evaluated by the number of cycles performed before the spallation of the ceramic layer at atmospheric pressure. The major difference lies in the thermal loads which are more or less representative of the thermal history experienced by the parts in service. It is also important to note that on the most common test benches reported below, the degradation mechanisms induced by the corrosive atmosphere of the engine are not yet well considered or well recreated. This section will, therefore, not focus extensively on this aspect.

4.1. Isothermal cycling test

The most common test in industry and laboratories is the isothermal cycling test. This test is relatively simple to implement and requires little equipment (furnace). It consists of three main steps (see Fig. 8):

1. Introduction of the samples into the oven at the targeted temperature (usually 1200°C), inducing a rapid temperature rise of the samples (<15min).
2. Stabilization at high temperature for 45 min (thermal stabilization, depending on the test conditions).
3. Removal of the samples from the oven, resulting in rapid cooling under compressed air to temperature values below 100°C (<15min).

With appropriate instrumentation, this test can be automated. Cycles are repeated until 10 to 20% of the coating is spalled [156]. Because the deposit and substrate are heated to the same temperature, the primary damage mechanisms without CMAS infiltration are controlled by growth of the TGO [115], and deformation of TGO/bond coat interface by ratcheting [157] or rumpling [158], in order to release accumulated stresses [157], [159]–[166].

CMAS particle deposition is typically performed by hand using a powder or paste on the samples before they are introduce into the oven [64], [115]. However, the amount deposited, about 30±10 mg·cm^{-2}, saturates the TBC system, and is not representative of real-world CMAS etching where deposition is done discontinuously over time.

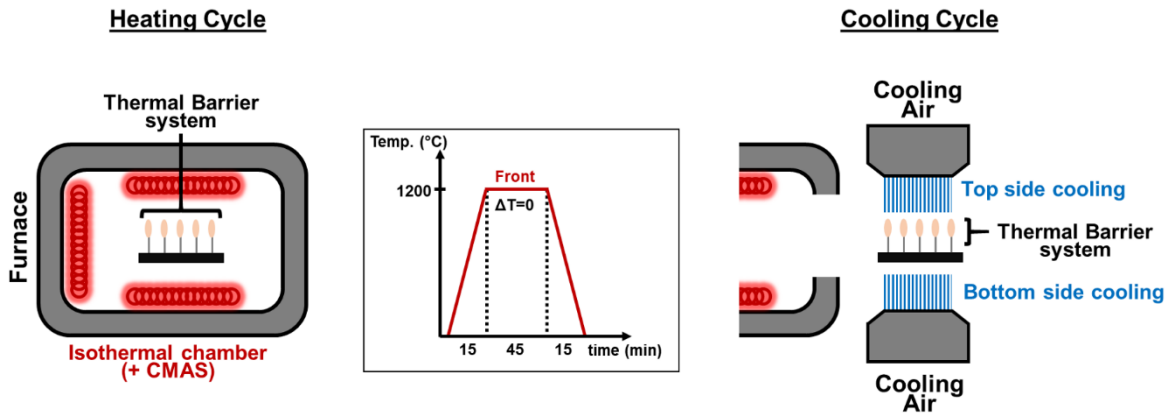

Fig. 8 Schematic diagram illustrating the principle of the isothermal cycling test

In summary, this test is particularly accessible and easy to implement but is not sufficiently representative, in terms of thermal and mechanical stresses, to correctly predict the behavior of TBC systems in service. This is why engine manufacturers, in collaboration with laboratories, have developed thermal gradient cycling tests with different CMAS deposition processes.

4.2. Thermal gradient cycling test

The considerable difference between the temperature at the outlet of the combustion chamber and the temperature used for internal cooling of the high-pressure turbine blades results in a significant thermal gradient in the TBC system. A.G. Evans and J.W. Hutchinson were the first, using a mechanical approach, to demonstrate the influence of this thermal gradient on the damage mechanisms of the TBC, with and without CMAS [134], [157]. Based on flight return parts, they were able to show, by modeling with realistic turbojet conditions, that the engine cooling phase is the most detrimental for the life of the coatings. There is also a clear correlation between the cooling kinetics and the delamination depth related to different damage mechanisms. The need to generate a thermal gradient in the TBC system to simulate realistic damage mechanisms under service conditions, is the main conclusion of this study [167].

There is not a single standard thermal gradient test bench. However, the common goal seems to be the generation of a thermal gradient in the topcoat that tends to $1°C \cdot \mu m^{-1}$. The main idea is to use, at the same time, a heat source and a cooling system, respectively in front of the topcoat and at the back of the substrate (see Fig. 9).

These test benches can be commonly classified (except in rare cases) into two groups according to the heat source used: laser or flame. On the one hand, the use of a CO_2 laser heat source [168]–[174] allows homogeneous heating on the top surface of the TBC by surface scanning [110], [175]. To ensure a thermal gradient inside the TBC, the back side of the sample is usually cooled with compressed air. This low-noise technology is particularly suitable for acoustic damage characterization [176]–[178]. On the other hand, the flame derived from an oxygen/fuel mixture (commonly gas [179] or kerosene [180]), is the most commonly used heat source, often coupled with compressed air cooling on the backside of the sample [181]–[183]. One of the most interesting advantages of these test benches is the ability to inject a controlled amount of

liquid or solid CMAS directly into the heat source, creating a corrosive environment similar to service conditions and simulating more realistic damage mechanisms.

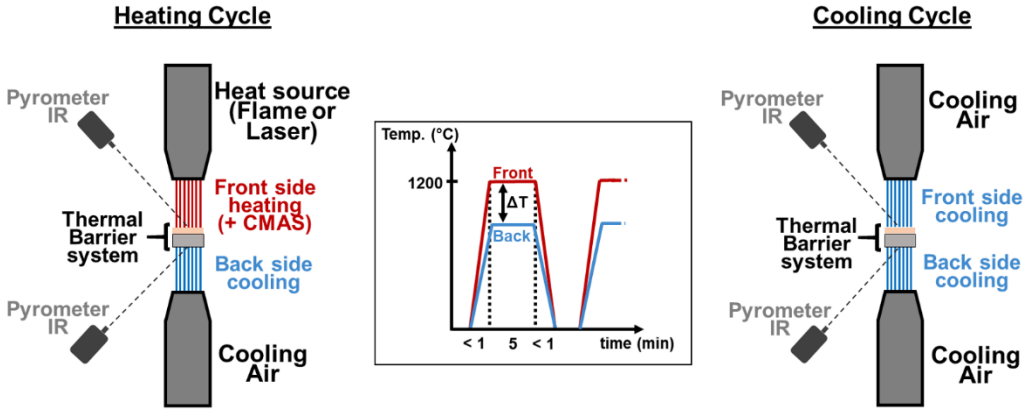

Fig. 9 Schematic diagram illustrating the principle of the thermal gradient cycling test

In both cases, the surface temperature of the coating is determined by means of pyrometric measurements or of infrared thermal cameras. In addition, a thermocouple is usually placed in the sample substrate. Knowing the thicknesses and conductivities of the different materials, it is thus possible to determine an interface temperature and deduce the thermal gradient induced across the TBC. While thermal gradient tests are more representative of flight conditions [184] and thus degradation mechanisms [185], they are also more complex to implement and require greater accuracy in temperature measurements. Infrared temperature measurements are particularly sensitive to the emissivity of the TBC material (typically YSZ). The maximum radiative emission area (>90%) for YSZ has been determine to be between 8 and 12.5 µm [186]. These wavelength ranges favor the use of pyrometric devices to have the most accurate temperature measurements possible. In addition, a variation of 55°C on the surface of the TBC can reduce the lifetime of the TBC by approximately 60% [187]. Therefore, an error in thermal measurement or a small thermal variation can have a relatively large impact on TBC damage [188]. Because the reaction kinetics between TBC and CMAS are strongly influenced by temperature, the surface temperature measurement should be as accurate as possible.

Table 2 gives an example of several test rigs developed by laboratories to study the behavior of TBC systems [179], [189], with or without CMAS infiltration. As observed, the heat sources, the cooling means, temperature ranges achieved, the type of loading considered and the possibility of implementing CMAS infiltration differ significantly from one rig to another [183].

Table 2 Non-exhaustive inventory list of gradient rig tests currently present in laboratories around the world

Laboratory / Institution	Country	Heat source	Heat source details	Sample temperature range	Sample shape	Cooling system	CMAS solicitation	Details of CMAS solicitation	Main solicitation
NASA [190]	USA	Flame	Natural gas/O_2	Up to 1650 °C	Multi-shapes (bar and flat)	Ambiant air (backside)	Not reported	-	High thermal flow + water vapor created by combustion
Stony Brook University [191]	USA	Flame	C_3H_8/O_2	Use 1250°C	Flat disk	Oil pump vacuum system (backside)	Yes	**CMAS solid** -- ash, radial injection trough the flame with powder feed system	CMAS + Thermal solicitation
Forschungszentrum Jülich GmbH [181], [192]	Germany	Flame	CH_4/O_2	1150°C to 1550°C	Flat disk	Compressed air (backside)	Yes	**CMAS liquid** -- liquid solution (0.1 wt.%) axial injection within the flame	CMAS + Thermal solicitation
Pprime [193], [194]	France	Flame	CH_4/O_2	300 to 1600 °C	Multi-shapes (tubular, flat and blade)	Compressed air (backside/internal)	Not reported	-	Mechanical (tensile/compressive) solicitation + High thermal flow
Marine new materials and related technology [123]	China	Flame	C_3H_8/O_2	Use 1300°C	Flat disk	Compressed air (backside)	Yes	**CMAS Paste** -- CMAS paste (2 wt.% - mixture of CMAS powde + ethanol) brushed every 2 cycles	CMAS + Thermal solicitation
Shanghai Institute of Ceramics [195]	China	Flame	C_3H_8/O_2	Use 1350±20 °C	Flat disk	Compressed air (backside)	Yes	**CMAS suspension** -- CMAS suspension at 25 wt.% deposited by atomisation at 7 $mg \cdot cm^{-2}$ before each test	CMAS + Thermal solicitation
India institute of technology [196]	India	Flame	Liquefied petroleum gas/O_2	Use 1400°C	Flat disk	Compressed air (backside)	Not reported	-	Thermal solicitation
University of california [110]	USA	Laser	2kW CO_2	Use 1300°C	Flat disk	Compressed air (backside)	Yes	**CMAS Paste** -- Powder + ethanol suspended mixture (CM(F)AS) (5 $mg \cdot cm^{-2}$)	CMAS + Thermal solicitation
National Research Council of Canada [170]	Canada	Laser	3kW CO_2 laser	Up to 1530°C	Flat disk	Compressed air (backside)	No	-	High thermal flow
Institute of Materials Research [197]	Germany	Micro engine	Kerosen	Up to 1600°C	Blade (simple form)	Conduction between blade to shaft which is internally cooled by air	Yes	**CMAS solid** -- Volcanic ash particle disperser (2 $mg \cdot m^{-3}$ - 4 $mg \cdot m^{-3}$)	CMAS + Erosion solicitation + Rotation

In summary, thermal gradient tests require sophisticated facilities and accurate temperature measurements (±20°C) of the surface but they can be more representative of flight conditions for TBC systems. The CMAS solicitations implemented during the cycles may vary according to the test rig (CMAS paste deposition, liquid or solid CMAS injection, etc...) but the dose of CMAS tested is often higher than in real service conditions [147]. The corrosive environment of the aircraft engine can also be more or less re-simulated depending on the nature of the heat source (see Table 2).

Finally, a thermal barrier coating must also allow the highest thermal gradient within it to effectively protect the underlying metal parts from the surrounding high temperatures (above 1200°C). Table 3 compares the temperature differences between the TBC surface and the TBC/substrate interface (ΔT), and the thermal gradient (grad T) within different types of thermal barrier coatings (APS, EB-PVD, SPS, SPPS and PS-PVD) obtained in the thermal gradient test. The thermal gradients obtained with the SPS coatings appear comparable to those obtained with the APS coatings. Nevertheless, the three values of thermal gradients given, in Table 3, for SPS are relatively different (between 0.61 and 0.98 $°C \cdot \mu m^{-1}$) contrary to the thermal gradient obtained by APS. This can be explained by the differences in microstructure (column density and porosity) on the studied TBCs [58] that can be obtained in SPS.

Table 3 Comparison of the thermal gradient obtained by gradient testing with different spraying process

Top Coat (process, µm)	ΔT (Top Coat) (°C)	grad T (Top Coat) ($°C \cdot \mu m^{-1}$)	Ref
7YSZ (APS, 600 µm)	466	0.78	[198]
YSZ (APS, 283 µm)	226	0.80	[199]
YSZ (APS, 272 µm)	286	1.05	[199]
YSZ (SPS, 245 µm)	241	0.98	[58]
YSZ (SPS, 257 µm)	227	0.88	[58]
YSZ (SPS, 317 µm)	194	0.61	[58]
YSZ + Al + Ti (SPPS, 200 µm)	177	0.88	[200]
YSZ porous (PS-PVD, 300 µm)	208	0.69	[201]
YSZ dense (PS-PVD, 330 µm)	200	0.61	[201]
7YSZ (EB-PVD, 350 µm)	247	0.71	[110]

However, it is interesting to note that the SPPS (solution precursor plasma spray) deposit referenced here, has a gradient comparable to that of the APS deposits. The SPS process offers comparable or superior thermal properties to the other processes.

Ultimately, the choice of the type of durability tests depends only on what one primarily wants to study. For example, for characterizing chemical damage on the surface TBC with CMAS, the isothermal cycling test may be sufficient and is simpler to implement. It should be kept in mind that this test is only partially representative of in-service chemical degradation because the dose of CMAS deposited at one time is often too high, but it provides a good understanding of the underlying chemical mechanisms by placing the test conditions in the most severe scenario. For more realistic stresses of in-service engine operating conditions with CMAS attacks, the thermal gradient test is preferable because the thermomechanical stresses are better simulated on such benches. With this test, residual stresses and a slower TGO growth are obtained, which brings the characterizations to a more realistic state of the operating conditions.

Nevertheless, there are few comparisons between isothermal and thermal gradient tests on the durability of TBCs under CMAS attack, especially for SPS coatings. The lifetime of SPS coatings in thermal gradient tests with CMAS stresses appear to be lower than the results obtained in isothermal tests [202]. The multiple degradation mechanisms (mainly CMAS) are not yet sufficiently well characterized to allow predictive optimizations of SPS coatings yet.

5. Current potential solutions against the CMAS attack

Currently, two development axes are studied by academic and industrial actors. They focus respectively on strategies related to materials or coatings, with possibility of interlocking. Both strategies have the same objectives: to radically improve the thermochemical and thermomechanical properties of TBCs in order to increase their resistance to the more difficult engine environments, including CMAS.

5.1. Material strategies

As previously mentioned, starting around 2000, many topcoat materials were investigated to overcome the limitations of yttria-stabilized zirconia in new generations of TBCs [140], [203],

[204]. The mapping shown Fig. 10 illustrates, in a non-exhaustive manner, the families of materials studied so far, to help identify potential materials with thermophysical properties equivalent to YSZ [205]–[207].

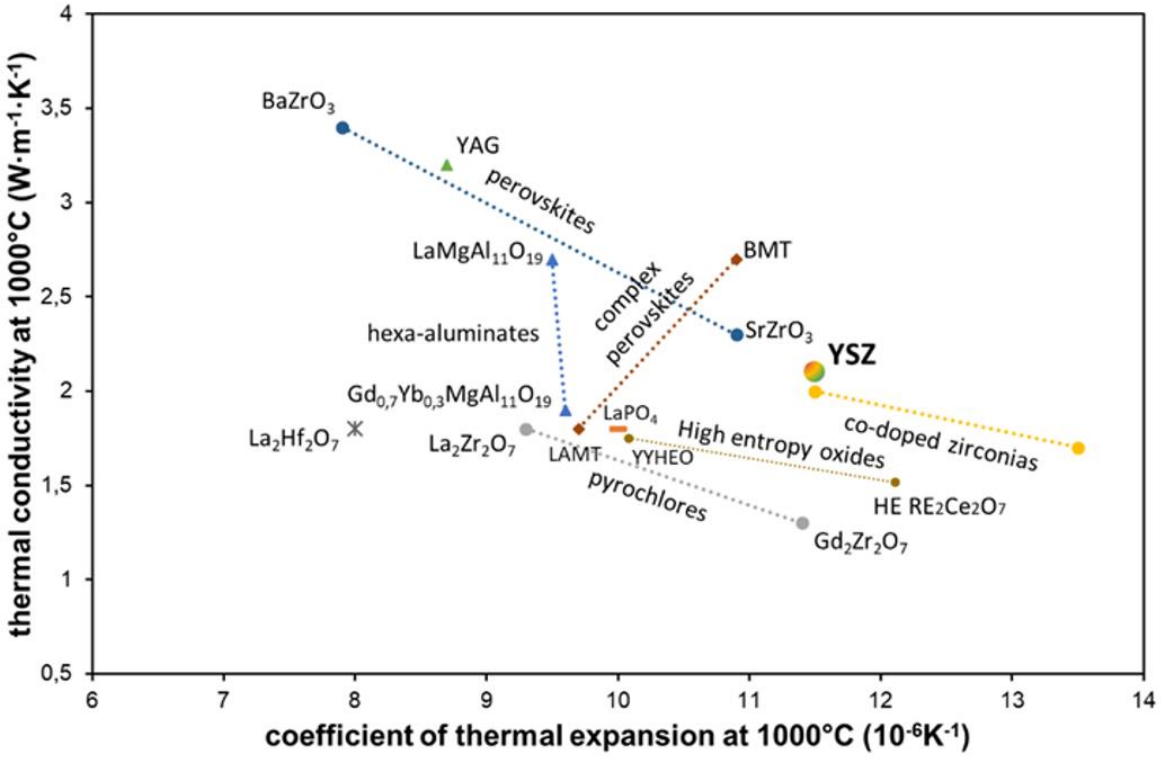

Fig. 10 Thermal conductivity of materials in each identified family as a function of their coefficient of thermal expansion, graph adapted and values taken from [205]–[211]

The co-doped zirconia RE_2O_3-ZrO_2 or $Y_2O_3(RE_1)_2O_3$-$(RE_2)_2O_3$-...-ZrO_2 with a fluorite/fluorine structure ("RE" stands for rare earth other than yttrium) as well as the pyrochlore family $RE_2Zr_2O_7$ have been identified as the materials offering the best compromise in thermal conductivity and coefficient of thermal expansion (CTE) [212], [213]. The thermal conductivity values are significantly lower than those of yttria-stabilized zirconia, with similar CTE. These materials may also exhibit sufficient resistance to high-temperature cyclic oxidation as well as good erosion resistance (for co-doped zirconia with several rare earths) to TBCs containing YSZ [212], [214], [215].

Coatings specifically containing $RE_2Zr_2O_7$ pyrochlores have been extensively studied in the literature, which means that there is a large data available on these coatings subjected to infiltration tests with different CMAS. This family of materials will be the subject of the following paragraphs.

The dissolution/precipitation mechanisms observed with $RE_2Zr_2O_7$ are close to those of YSZ in CMAS, i.e., RE^{3+} cations (RE: La → Yb) have a marked basic role and act preferentially as lattice-modifying oxides. The larger their radius, the more basic the cations are, the more soluble they are in acidic media, such as fused silicates. They facilitate depolymerization of this medium and initiate the formation of crystalline silicate phases, which equilibrate and stabilize in temperature, such as the cyclosilicates $Ca_3RE_2(Si_3O_9)_2$, orthosilicate apatite phases $Ca_2RE_8(SiO_4)_6O_2$ or the disilicate pyrochlores $RE_2Si_2O_7$ [125], [216]–[222]. Significant distortions can appear in the crystal structure of these new compounds. They are strongly correlated with the ionic radius of the rare earth, which has an impact its coordination number in the crystal structure.

The smallest cations, such as Yb^{3+} and Dy^{3+}, behave similarly to Y^{3+}, and stabilize a mixture of the three silicate phases mentioned above, with preferential formation and stability of cyclosilicates. Perrudin et al. [130] showed that these cyclosilicates have a lower solubility in silicate glasses than other types of silicate by-products, meaning that less RE^{3+} is dissolved in the melt to form this phase (RE:Si ratio = 0.33). This results in less recession of the coating containing these rare earths when exposed to CMAS, due to the lower solubility of the cations, as has been observed in other studies [129], [216], [223]. Compounds rich in Gd^{3+}, Sm^{3+} and Nd^{3+} form the apatite phase predominantly (RE:Si ratio = 1.33), with coating recession increasing with the size of the rare-earth ionic radius, due to the higher solubility of these cations in CMAS [129], [223]. Perrudin et al. [130] also noted a discontinuity in the relationship between cation field strength and solubility/basicity behavior for the smaller cations Yb^{3+} and Dy^{3+}, for short periods of exposure with CMAS (<4hrs at 1200°C), compared to compounds with the larger cations.

This could be due to the concomitant formation and stability during this time period of the RE:Si equilibrium phase $Yb_2Si_2O_7$ in the latter case. Therefore, the "anti-CMAS" chemical potential of RE-doped zirconia is highly dependent on the stability of the crystallized silicate phases and the solubility of the RE^{3+} cations in the glass.

In addition, all studies on the interaction between RE-zirconia and CMAS lead to the conclusion that the rate of sealing of coatings' porosities must be a main factor for the development of an effective "anti-CMAS" coating. The introduction of Gd species into the CMAS-TBC environment, especially through $Gd_2Zr_2O_7$ ("GZ") coatings, presents the best compromise among RE-zirconias for the reactivity with CMAS (cation field strength and solubility/basicity) and for the sealing mechanism in this respect. In this case, an interface layer between the TBC and CMAS is formed within one min of CMAS infiltration into the coating, between 1150 and

1200°C [131], [224]. This layer effectively seals the porosities with a surface opening of less than 1 µm [225] and typically consists of a "dense" layer composed of weakly Gd-doped zirconia nodules and needle-like Gd-apatite crystals [140], [226]. Dolmaire et al. [227] also observed the presence of a thin layer of Gd-disilicate species at this interface, the formation and stability of which is concomitant in temperature with the formation and stability of Gd-apatites and depends on the Si:Ca ratio of the starting mixtures of oxides derived from CMAS. This concomitant precipitation of Gd-disilicates and Gd-apatites could be due to the intermediate basic character of Gd^{3+} in CMAS melts. Dolmaire et al. established a diffusion model similar to that one proposed in Fig. 6 of this chapter, in which the presence of a thin layer of Gd-disilicate at the $(liquid)_{CMAS}$ / $(Gd\text{-}apatite)_{crystals}$ interface appears to slow down the interdiffusion of ionic species at the interface and may explain why Gd-based coatings exhibit such a good compromise. This specificity of GZ reactivity leads to both a lower level of coating surface recession, compared to RE-zirconia containing larger RE cations, and a shallower depth of infiltration into the coating volume compared to RE-zirconia containing smaller RE cations [129].

5.2. Coating strategies

The choice of materials is of paramount importance in the "anti-CMAS" strategy, but the coating morphology should not be neglected either. Indeed, depending on the coating treatment, variable porosity levels and/or controlled macro-defects such as columns or wide cracks will be obtained. These process-dependent features influence the degree of degradation of CMAS infiltration, as open coating structures favor the flowability of identical CMAS into the coating compared to denser structures [115], [191], [225], [228].

Yang et al. [228] compared the spreading of volcanic ashes on YSZ coatings produced by APS (highly porous lamellar structure) and EB-PVD (columnar structure with interconnected inter-columnar spaces) at different temperatures (from 1200 to 1600°C). They showed that the dynamic spreading rate of spherical volcanic ashes on TBC is strongly influenced by the melt viscosity, concentration gradient and coating morphology. When the melt reaches the target temperatures (i.e 1200, 1400 or 1600°C), the low viscosity (> 362 Pa·s at 1200°C, 80.7 Pa·s at 1400°C, 10.3 Pa·s at 1600°C) favors interactions with the surface and microstructure of the coating. According to their observations, the coating morphology then becomes the dominant

factor in controlling the spreading of volcanic ashes. Surface spreading is more extensive on the APS coating surface because the surface roughness is higher. This factor increases the wettability of the melt due to the large capillary forces. Comparatively, the vertical and lateral subsurface infiltration depths of the CMAS melt are higher in EB-PVD coatings at the same melting stage due to the higher pore connectivity (inter-column spaces) while the spreading front on the surface is less extensive due to the lower surface roughness. Therefore, they propose that producing YSZ coatings with minimal surface roughness (promoting non-wetting behavior) and low-connected porosity (attenuating infiltration depths) is more likely to withstand CMAS degradation in temperature and for a longer period of time.

This proposal is in line with the overall development trends of TBCs that attempt to trade-off thermomechanical requirements for the coating with mitigation of CMAS degradation. Two main architectural strategies can be distinguished among these: the development of multilayer topcoats or the texturing of coating surfaces [191], [209], [229].

Specifically, attempts have been made to combine the thermomechanical properties of yttria-stabilized zirconia with the "anti-CMAS" behavior of other materials, either through reactivity to CMAS and associated chemical sealing mechanisms or through a non-wetting effect on CMAS [23], [208].

As previously reported, the $RE_2Zr_2O_7$ pyrochlore materials have been identified as excellent candidates to replace YSZ in TBCs, particularly GZ which exhibits the best reactivity to CMAS infiltration among them. However, in a traditional TBC system, GZ reacts at temperature with the alumina that forms between the ceramic coating and the (Ni, Pt)-Al bond coat, resulting in the formation of $GdAlO_3$ phases detrimental to the oxidation protection of the bondcoat [230], [231]. GZ coatings also exhibit poor thermomechanical properties compared to YSZ coatings in isothermal cyclic oxidation and erosion resistance tests [69], [215], [232], [233]. Therefore, efforts have been made to develop multilayer YSZ/GZ coatings to combine the beneficial properties from both materials and counteract the mechanical weaknesses of GZ [191], [234]–[236]. In these architectures, YSZ is always the first ceramic layer above the bondcoat to prevent reactions between GZ and the TGO.

The work of Mahade et al. [69], [156], [233]–[235] can be particularly highlighted with respect to the study of thermomechanical properties of SPS coatings with multilayer YSZ/GZ architectures. Their experiments using isothermal furnaces or a burner rig show that higher oxidation resistance and thermal shock resistance can be achieved with double or triple-layer

YSZ/GZ SPS coatings compared to SPS coatings comprising only a single layer of YSZ [156], [234], [235]. Notably, the thickness of the YSZ layer in the double-layer coatings is almost inversely proportional to the TBC lifetime in their burner rig test conditions (thermal gradient of 200°C in the samples with the TBC surface exposed to 1350°C during the heating stage). Thicker layers of GZ in double-layer coatings have a beneficial impact on oxidation resistance. Mahade et al. hypothesize this is likely due to the lower thermal conductivity of GZ compared to YSZ, which results in slower growth of the TGO film between the topcoat and the metal bond coat, which is a known factor in TBC failure. The lower fracture toughness of GZ would be the primary factor in the faster failure of the coating with the thickest YSZ, they hypothesize. In this case, the GZ layer crumbles early in the test, resulting in higher thermomechanical stresses in the rest of the YSZ coating and to lower thermal shock resistance.

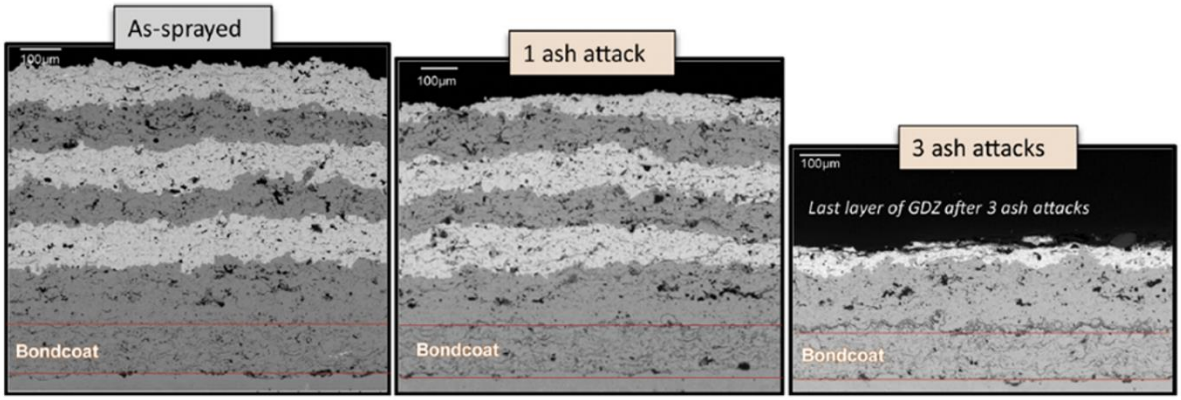

Fig. 11 Multilayer coating consisting of GZ (light layer) and YSZ (dark layer) subjected to successive attacks of lignite ash in a thermal gradient test (burner rig) [191]

YSZ/GZ multilayer coatings have also been tested against CMAS attack in thermal shock or infiltration tests under isothermal or thermal gradient conditions [191], [228], [237]. For example, the results of Gildersleeve et al. [191] show that double-layer YSZ/GZ APS coatings effectively resist a single exposure to lignite ash (35 mg·cm^{-2} of CMAS) during thermal shock tests featuring a thermal gradient of 250°C in the samples during the heating phase (TBC surface held at 1250°C in a burner rig). Other attacks lead to the complete spallation of the APS GZ layer during cooling and the mechanical degradation (cracks) of the underlying YSZ layer. To counteract this phenomenon, they developed a multilayer YSZ/GZ APS coating with alternate layers of each, keeping a GZ layer on top (Fig. 11). The spray parameters were adapted to produce porous layers of each material in order to control the thermomechanical stresses after each CMAS attack. Indeed, they noticed with single and double-layer coatings that sufficiently high porosity forced delamination between each layer and reduced the thickness of

CMAS infiltration, compared to denser coatings with vertical cracks. These two microstructural observations were also highlighted by Morelli et al. in their studies of CMAS infiltration at 1250°C and thermal shocks resistance of YSZ/GZ APS coatings at 1100°C in isothermal furnaces [236]. The results obtained after several CMAS attacks under a thermal gradient show that the porous multilayer YSZ/GZ system is effective in withstanding several attacks while preserving the advantages of the double-layer system (i.e., retaining the combination of an anti-CMAS layer with a thermomechanical compliant underlayer), although the inevitable delamination of the infiltrated top layers (Fig. 11).

Zhou et al. [237] studied the same phenomena with YSZ/GZ multilayer coatings comprising a porous APS YSZ layer and columnar or dense SPS GZ top layers (Fig. 12). Their results highlight a significantly higher thermal shock resistance under thermal gradients of the APS/SPS multilayer coatings compared to single APS YSZ TBCs (TBC surfaces held at 1400°C with a thermal gradient of 300°C during the heating stage). They infer this is due to the greater strain tolerance improved by the SPS columns and the lower thermal conductivity of GZ. The addition of CMAS attacks during these thermal shocks shows that the best thermal resistance to thermal shock and infiltration comes from the triple-layer coating containing a densified SPS GZ topcoat with vertical as-sprayed cracks (Fig. 12 b and d). The CMAS infiltration depth remains the same in the YSZ/GZ coatings tested independently of the microstructures of the GZ top layers under their test conditions (TBC surfaces held at 1250°C with a thermal gradient of 250°C within the samples). All APS/SPS multilayer coatings failed under cold shocks (spallation of the GZ layers from cracks within the GZ layers). The differences in thermal shock resistance between the multilayer YSZ/GZ coatings tested could be due to the better thermomechanical properties of the triple-layer YSZ/GZ coating. In the latter case, it has a higher fracture toughness and elastic modulus than the other type of multilayer coating tested which could allow the coatings to withstand longer.

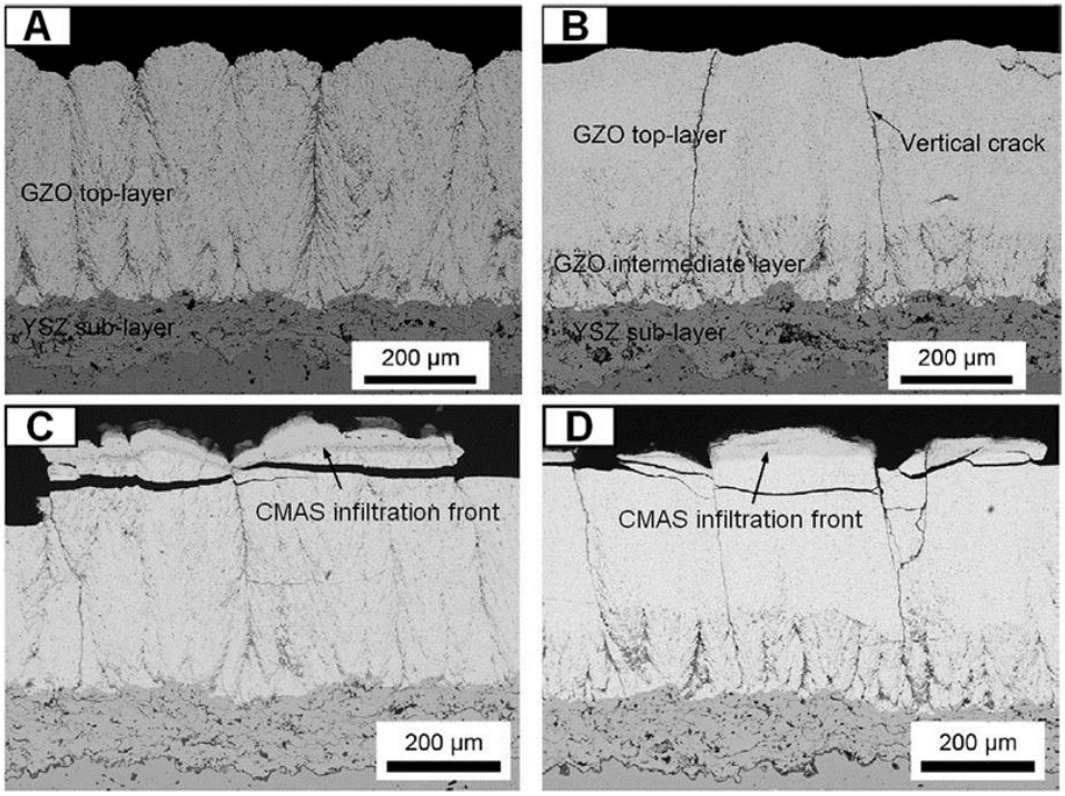

Fig. 12 Multilayer coating consisting of SPS GZ (light layers) and APS YSZ (dark, porous layers) subjected to CMAS attacks in a thermal gradient test (burner rig). A and B show the as-sprayed coatings, C and D show the SPS GZ/APS YSZ double-layer (C) and the triple-layer SPS-dense GZ/SPS GZ/APS YSZ (D) coatings after CMAS infiltration and delamination [237]

Ultimately, this strategy capitalizes on the sacrificial effect of GZ reactivity to CMAS. The TBC will ineluctably delaminate, whether as a result of successive CMAS attacks or other extrinsic degradations. Such multilayer TBCs are interesting because they should allow for a longer service lifetime before inevitable maintenance.

Several patents mention the non-wetting behavior to CMAS of topcoats including noble metals, carbides, borides, … [238], [239] but very few studies have been published on these materials to corroborate these claims [121], [240]. However, recent studies have emphasized on the prominent role of surface texturing and geometry in promoting a non-wetting behavior to CMAS. Strategies used lie in optimizing deposition processes or in post-process modifications such as polishing or laser-texturing TBCs [154], [241]–[247].

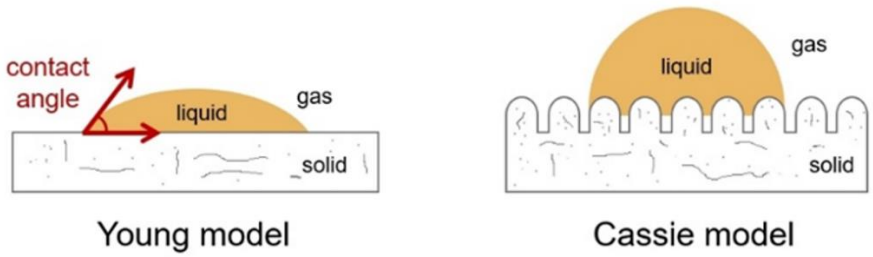

Fig. 13 Wetting models

W. Qu et al. [248] tested the wettability of CMAS on single cubic crystals of YSZ with three different orientations. Their study shows that, during CMAS attack, the YSZ nodules forming at the $(liquid)_{CMAS}$ / $(YSZ)_{crystal}$ interface into inverted trapezoids are favorable for maintaining a higher contact angle and limiting the spreading rate of CMAS below 1230°C in air. This microgeometry of the re-precipitated zirconia nodules was a characteristic of YSZ crystals oriented in the {1 0 0} direction. As they report, this experimental result is contrary to first-principle descriptions of Young wetting model predicting that the {1 1 1} cubic crystal should lead to the lowest CMAS spreading velocity and higher contact angle, due to the limited surface energy of the crystal relative to the {1 0 0} plane (65 meV·Å^{-2} and 109 meV·Å^{-2} respectively). They conclude that the microgeometry formed at the $(liquid)_{CMAS}$ / $(YSZ)_{crystals}$ interface during infiltration is the main factor in the wetting behavior of CMAS with YSZ. This microgeometry significantly weakens the action of surface energy. They deduced that the interface composed of inverted trapezoids of YSZ could promote a composite contact between the molten CMAS melt, the YSZ nodules and the air trapped at the interface (Cassie wetting model, Fig. 13). This hypothesis would explain the unexpected wetting behavior, due to the lower surface energy between the melt and the gas. Contact angle calculations using the Cassie model seem to confirm this experimental result.

Other studies have reported similar effects of surface geometry on the non-wetting behavior to CMAS for several surface structural scales [154], [241]–[247]. Some of the experimental data described below have been summarized in Fig. 14.

For example, Yang et al. [243] compared several CMAS spreading rates on APS YSZ coatings with increasing surface roughness using a temperature wettability test (in unknown atmosphere). They observed on all samples and with all types of CMAS (natural volcanic ash, industrial by-product fly ash, synthetic CMAS) a short period of non-wetting behavior (contact angles greater than 120° between coating and melt) before the viscosity of the CMAS melt reaches a value low enough to initiate spreading on all YSZ coatings (between 1200 and

1250°C). Furthermore, as the coating roughness decreases, this non-wetting behavior extends over time, regardless of the chemical composition of the CMAS. The wetting area of the melts also decreases with the reduction in surface roughness over the same time. This has an impact on the lasting spreading area of the melts at higher temperatures. Yang et al. observed the smallest spreading zones for YSZ coatings with the highest contact angle with the melts during the previous non-wetting step. Guo et al. [154] demonstrated the same phenomena in their study comparing the wetting behavior of CMAS on YSZ, $GdPO_4$ and $LaPO_4$ coatings with different surface roughnesses. They also noted advantages related to the initial coating chemistry for similar surface roughnesses, with $REPO_4$ coatings retaining higher contact angles with CMAS than YSZ coatings (nearly 70° for $GdPO_4$ vs. to 11° for YSZ polished bulks after 1h at 1250°C in air). They attribute these differences to lower surface energies of $REPO_4$. The precipitation of Gd or La-compounds at the $(liquid)_{CMAS}$ / $(solid)_{coating}$ interface could also play a role into this non-wetting behavior by modifying the topography of the interface, in a similar fashion than Qu et al. experiments reported previously, but this aspect was not investigated by the authors.

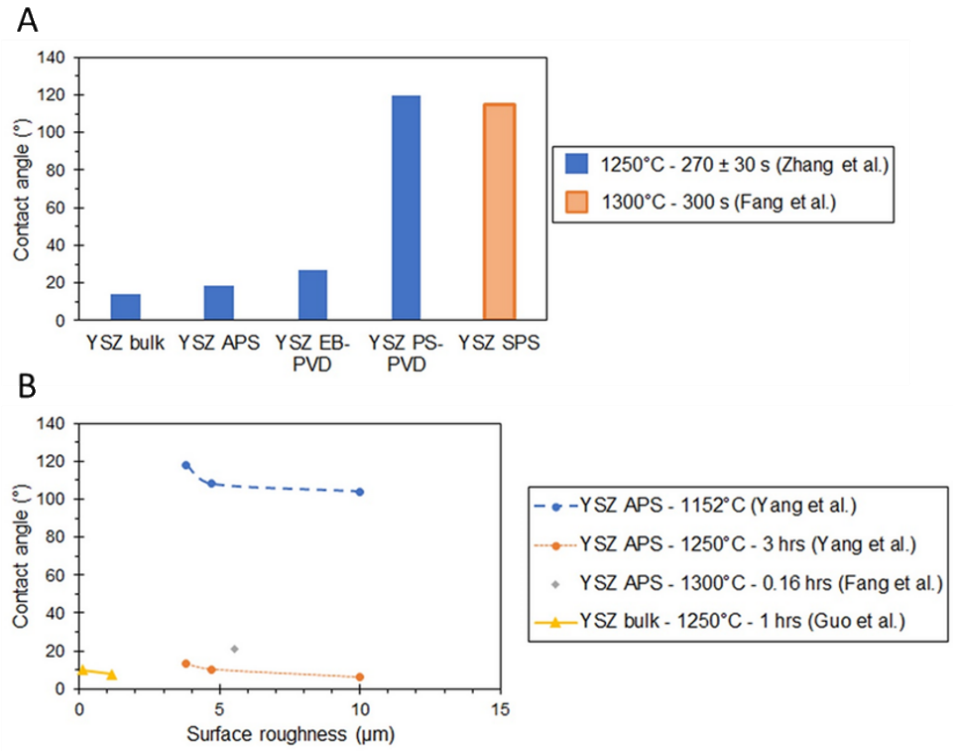

Fig. 14 Contact angles between YSZ coatings and CMAS as a function of (A) coating processes and (B) surface roughness, data collected from [154], [242], [243], [249]

Zhang et al. [242] investigated the potential effect of multiscale roughness on the wettability of CMAS by comparing the spreading of CMAS at 1250°C (unknown atmosphere) on YSZ coatings produced by different techniques (i.e., EB-PVD, APS and PS-PVD). They found out that PS-PVD dual-scale surface roughness, comprising of round-shaped micro-protuberances (diameter between 1 and 7 µm) on which branch-like nano-scale tips are observed (tip diameter between 50 and 100 nm), is beneficial for the promotion of a "CMAS-superphobic" surface in the first minutes of CMAS melting (Fig. 14). The gas, trapped between the multiscale tips of the coating and the molten CMAS, could be the main driver of the observed superphobic surface behavior (contact angle of about 120°), based on surface energy calculations.

Such surface texturing, achieved through the characteristics of the PS-PVD process, can also be achieved by SPS, using the right set of spraying parameters. Fang et al. [249] investigated this, examining the infiltration of CMAS on a YSZ coating consisting of a columnar layer produced by SPS on an APS layer. After 5 minutes at 1300°C, they measured a contact angle of 115° between CMAS and the YSZ surface, which they attribute to the micro and nano-scale morphology of the coating surface, analogous to PS-PVD coatings. However, the melt eventually wets the surface of YSZ coating surface in all cases.

Other studies focusing on laser-glazed or laser-ablated TBCs report similar results to either CMAS wetting behavior or infiltration into TBCs thanks to a significant decrease in surface roughness and entry points [250], [251] or a promotion of a three-phase contact angle (liquid CMAS, solid TBC and gases) [246], [247]. Study by Guo et al. [246] especially insists on a lasting non-wetting behavior of laser-ablated coatings (contact angle around 105° at 1200°C) after thermal ageing (10hrs at 1300°C), which is a critical variable considering the TBC environment. They explain this lasting effect by the higher concentration of nanoparticles covering the coating tips after coating re-melting during laser-ablation, compared to as-deposited PS-PVD coatings (which retain a contact angle of 90° at 1200°C after thermal ageing). Therefore, they achieved this result thanks to an enhanced micro and nano-scale surface morphology as underlined before.

In summary, an ideal TBC exhibiting anti-CMAS behavior and conformal thermomechanical properties should have the following characteristics:

- A textured surface containing micro and nano-scale tips to promote "CMAS-superphobic" behavior to slow down CMAS wetting over time and temperature through gas entrapment at the $(liquid)_{CMAS}$ / $(solid)_{coating}$ interface.

- A low surface roughness at the macroscopic scale to inhibit capillary forces that drive molten CMAS into the porosities of the coating.
- A multilayer architecture comprising at least:
    - A GZ top layer to limit the depth of CMAS infiltration into the TBC and limit coating recession, due to the high reactivity at the $(liquid)_{CMAS}$ / $(GZ)_{coating}$ interface.
    - A GZ top layer dense enough to limit CMAS entry points during infiltration and to reduce the thermal conductivity of the coating.
    - A lower YSZ layer composed of porous columns to effectively accommodate thermomechanical stresses and further lower the thermal conductivity.

This architecture and properties can be achieved by SPS (Fig. 15) by optimizing all the parameters. The multiscale microstructure and diversity of coating morphologies offered by the SPS process should allow coatings to be tailored to fulfill the anti-CMAS strategies described: a "CMAS-superphobic" surface behavior to limit CMAS attack with an underlying multilayer coating with conformal thermochemical (high reactivity to CMAS) and thermomechanical properties. Further studies are needed to test these hypotheses under realistic service conditions and compare the available data.

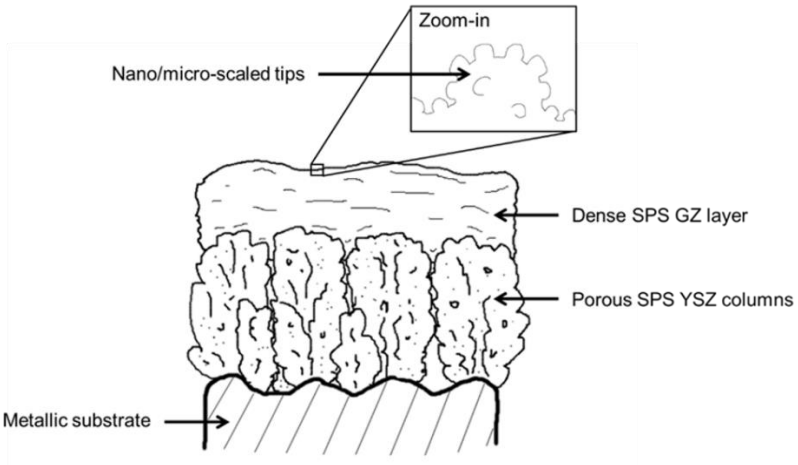

Fig. 15 Proposed coating architecture and materials to improve the anti-CMAS and thermomechanical properties of future TBCs, using only the SPS process

In particular, research on CMAS infiltration in YSZ/GZ multilayer coatings has not yet been performed using coating architectures comprising only of SPS layers, as far as we know. This

research would provide new insights into the wetting behavior of CMAS during infiltration and the thermomechanical behavior of SPS multilayer coatings.

6. Conclusion

As the challenges of climate change continue to mount, it becomes increasingly crucial to reduce the polluting emissions of air transportation. To this end, engine manufacturers are exploring various solutions, and one of them involves increasing the efficiency of aircraft engines by raising the temperature at the outlet of the combustion chamber. However, this poses challenges for the lifespan of thermal barrier coatings. During flight, engines ingest sand and volcanic ash particles known as CMAS, which can accumulate on the thermal barrier coating among other possibilities (erosion, clogging). The thermochemical properties of these particles, such as flowability and basicity, determine the extent to which they infiltrate the coating's porosity, leading to chemical degradation of the yttria-stabilized zirconia. During engine cooling phases, these particles vitrify, causing mechanical stresses in the coating and promoting the initiation of cracks parallel to the interface, ultimately leading to spalling of the thermal barrier.

To address these premature flaking issues, various strategies are proposed in the literature, such as using materials that slow down the infiltration of particles (e.g., gadolinium zirconate) or modifying the surface roughness to make the coating “CMAS-superphobic”. However, it is necessary not to degrade the main properties of the topcoat, which are low thermal conductivity and the ability to accommodate thermal stresses. It has been widely demonstrated that these properties are controlled by the microstructure of the yttria-stabilized zirconia topcoat. In this chapter, the authors explored how the suspension plasma spray (SPS) process can address these challenges while remaining economically viable.

Indeed, the SPS process allows great versatility in microstructure and could be used to coat both components of the combustion chamber and high-pressure turbines, while being less expensive than the EB-PVD process. That is why many engine manufacturers are interested in developing these SPS thermal barrier coatings.

However, properly characterizing the in-service behavior of these new thermal barrier coatings is necessary to consider their future industrialization. To date, two main tests are used: the

isothermal test and the thermal gradient test. The latter is more representative but more complex to implement, especially regarding temperature control. For both tests, the CMAS solicitation is not very representative of what happens in service because the topcoat is saturated with CMAS while infiltration should occur over time. Moreover, each test bench is developed separately, and the results cannot be correctly compared. The question then arises of how to properly characterize these thermal barriers. By refining the characterization, it will be easier to determine which composition, microstructure and architecture are the best adapted to the conditions the TBC are subjected in service. The SPS process parameters could then be optimized to achieve the desired coating characteristics. However, this requires an understanding of the interactions between the materials and process parameters, which are generally closely related to each other. This understanding is aided by the use of sensors to study in-flight material processing and coating growth and/or numerical process models. Sensors and digital models, along with massive data collection, also form the basis for developing digital twins to mimic the SPS process. Digital process twins will enable much faster coating development for parts with complex geometry and prediction of coating characteristics. Digital twins and big data can also be used to predict the life of different parts of an aircraft engine operated with different fuels in different environments allowing for rapid screening and selection of promising material configurations. Ultimately, this integration of SPS, big data, and digital twins could enable the development of TBCs with increased performance and durability, and reduce the development time and cost of TBC systems.

Acknowledgment

This work received no specific grant from any funding agency in the public or commercial sectors but M.G. would like to thank SAFRAN for the funding of his thesis. The authors of IRCER and ONERA would also like to thank the New Aquitaine region and SAFRAN for their support to the development of new generation coatings for aeronautics.

References:

[1] H.-O. Pörtner et al., Eds., Climate Change 2022: Impacts, Adaptation and Vulnerability. Contribution of Working Group II to the Sixth Assessment Report of the Intergovernmental Panel on Climate Change. 2022.

[2] L. Atwoli et al., 'Call for Emergency Action to Limit Global Temperature Increases, Restore Biodiversity, and Protect Health', N Engl J Med, vol. 385, no. 12, pp. 1134–1137, Sep. 2021, doi: 10.1056/NEJMe2113200.

[3] Airbus, The Boeing Company, Dassault Aviation, GE Aviation, Rolls-Royce, Safran and United Technologies Corporation, 'The Sustainability of Aviation', NVI Joint statement.

[4] 'Air France-KLM CO_2 emissions reduction targets for 2030 approved by the Science Based Targets initiative (SBTi)* | AIR FRANCE KLM'. https://www.airfranceklm.com/en/newsroom/air-france-klm-co2-emissions-reduction-targets-2030-approved-science-based-targets-0 (accessed Feb. 12, 2023).

[5] 'Aviation – Analysis', IEA. https://www.iea.org/reports/aviation (accessed Feb. 12, 2023).

[6] Stan Shparberg and Bob Lange, 'Global Market Forecast 2022'. Airbus presentation.

[7] Mosely, 'As Air Travel Rebounds, Boeing Forecasts Demand for More than 41,000 New Airplanes by 2041', MediaRoom, 2022. https://boeing.mediaroom.com/2022-07-16-As-Air-Travel-Rebounds,-Boeing-Forecasts-Demand-for-More-than-41,000-New-Airplanes-by-2041 (accessed Feb. 12, 2023).

[8] Fred Pearce, 'How Airplane Contrails Are Helping Make the Planet Warmer', Yale E360. https://e360.yale.edu/features/how-airplane-contrails-are-helping-make-the-planet-warmer (accessed Feb. 12, 2023).

[9] 'ATAG'. https://www.atag.org/our-activities/climate-change.html (accessed Feb. 12, 2023).

[10] IATA (77th IATA Annual General Meeting), 'Resolution on the industry's commitment to reach net zero carbon emissions by 2050', 2021.

[11] Advisory Group for Aerospace Research & Development (AGARD), Advanced Aero-Engine Concepts and Controls. 1996. Accessed: Feb. 12, 2023. [Online]. Available: http://archive.org/details/DTIC_ADA311466

[12] M. R. Dorfman, G. Dwivedi, C. Dambra, and S. Wilson, 'Perspective: Challenges in the Aerospace Marketplace and Growth Opportunities for Thermal Spray', J Therm Spray Tech, vol. 31, no. 4, pp. 672–684, Apr. 2022, doi: 10.1007/s11666-022-01351-x.

[13] S. Paquin, R. P. Cariou, T. M. Flamme, and A. B. V. Rollinger, 'Turbine blade having an improved structure', WO2018189434A3, Dec. 20, 2018

[14] A. B. V. Rollinger, R. P. Cariou, T. M. Flamme, and S. Paquin, 'Turbine blade comprising a cooling circuit', US10844733B2, Nov. 24, 2020

[15] S. T. Vagge and S. Ghogare, 'Thermal barrier coatings: Review', Materials Today: Proceedings, vol. 56, pp. 1201–1216, Jan. 2022, doi: 10.1016/j.matpr.2021.11.170.

[16] A. Feuerstein, J. Knapp, T. Taylor, A. Ashary, A. Bolcavage, and N. Hitchman, 'Technical and Economical Aspects of Current Thermal Barrier Coating Systems for Gas Turbine Engines by Thermal Spray and EBPVD: A Review', J Therm Spray Tech, vol. 17, no. 2, Art. no. 2, Jun. 2008, doi: 10.1007/s11666-007-9148-y.

[17] A. Vardelle, C. Moreau, N. J. Themelis, and C. Chazelas, 'A Perspective on Plasma Spray Technology', Plasma Chem Plasma Process, May 2015, doi: 10.1007/s11090-014-9600-y.

[18] N. Kumar, M. Gupta, D. E. Mack, G. Mauer, and R. Vaßen, 'Columnar Thermal Barrier Coatings Produced by Different Thermal Spray Processes', J Therm Spray Tech, vol. 30, no. 6, pp. 1437–1452, Aug. 2021, doi: 10.1007/s11666-021-01228-5.

[19] B. Bernard, L. Bianchi, A. Malié, A. Joulia, and B. Rémy, 'Columnar suspension plasma sprayed coating microstructural control for thermal barrier coating application', Journal of the European Ceramic Society, vol. 36, no. 4, Art. no. 4, Mar. 2016, doi: 10.1016/j.jeurceramsoc.2015.11.018.

[20] A. Kebriyaei, M. R. Rahimipour, M. Razavi, and A. Alizade Herfati, 'Effect of Solution Precursor on Microstructure and High-Temperature Properties of the Thermal Barrier Coating

Made by Solution Precursor Plasma Spray (SPPS) Process', J Therm Spray Tech, Oct. 2022, doi: 10.1007/s11666-022-01470-5.
[21] G. Pujol, F. Ansart, J.-P. Bonino, A. Malié, and S. Hamadi, 'Step-by-step investigation of degradation mechanisms induced by CMAS attack on YSZ materials for TBC applications', Surface and Coatings Technology, vol. 237, pp. 71–78, Dec. 2013, doi: 10.1016/j.surfcoat.2013.08.055.
[22] R. G. Wellman and J. R. Nicholls, 'A review of the erosion of thermal barrier coatings', J. Phys. D: Appl. Phys., vol. 40, no. 16, p. R293, Aug. 2007, doi: 10.1088/0022-3727/40/16/R01.
[23] M. P. Bacos et al., '10 Years-activities at Onera on advanced thermal barrier coatings', AerospaceLab, no. 3, Art. no. 3, 2011.
[24] R. Darolia, 'Thermal barrier coatings technology: critical review, progress update, remaining challenges and prospects', International Materials Reviews, vol. 58, no. 6, pp. 315–348, Aug. 2013, doi: 10.1179/1743280413Y.0000000019.
[25] P. L. Fauchais, J. V. R. Heberlein, and M. I. Boulos, Thermal Spray Fundamentals. Boston, MA: Springer US, 2014. doi: 10.1007/978-0-387-68991-3.
[26] A. Vardelle et al., 'The 2016 Thermal Spray Roadmap', Journal of Thermal Spray Technology, vol. 25, no. 8, Art. no. 8, Dec. 2016, doi: 10.1007/s11666-016-0473-x.
[27] C. Ruelle, S. Goutier, V. Rat, A. Keromnes, C. Chazelas, and E. Meillot, 'Study of the electric arc dynamics in a cascaded-anode plasma torch', Surface and Coatings Technology, 2023.
[28] E. Pfender, 'Fundamental studies associated with the plasma spray process', Surface and Coatings Technology, vol. 34, no. 1, pp. 1–14, Jan. 1988, doi: 10.1016/0257-8972(88)90083-7.
[29] R. Zhukovskii, C. Chazelas, A. Vardelle, and V. Rat, 'Control of the Arc Motion in DC Plasma Spray Torch with a Cascaded Anode', J Therm Spray Tech, vol. 29, no. 1, pp. 3–12, Jan. 2020, doi: 10.1007/s11666-019-00969-8.
[30] P. Fauchais, J. F. Coudert, M. Vardelle, A. Vardelle, and A. Denoirjean, 'Diagnostics of thermal spraying plasma jets', JTST, vol. 1, no. 2, pp. 117–128, Jun. 1992, doi: 10.1007/BF02659011.
[31] M. Vardelle, A. Vardelle, A. C. Leger, P. Fauchais, and D. Gobin, 'Influence of particle parameters at impact on splat formation and solidification in plasma spraying processes', JTST, vol. 4, no. 1, pp. 50–58, Mar. 1995, doi: 10.1007/BF02648528.
[32] L. Blanchi, A. Grimaud, F. Blein, P. Lucchèse, and P. Fauchais, 'Comparison of plasma-sprayed alumina coatings by RF and DC plasma spraying', JTST, vol. 4, no. 1, pp. 59–66, Mar. 1995, doi: 10.1007/BF02648529.
[33] G. Mauer, R. Vaßen, and D. Stöver, 'Comparison and Applications of DPV-2000 and Accuraspray-g3 Diagnostic Systems', J Therm Spray Tech, vol. 16, no. 3, pp. 414–424, Sep. 2007, doi: 10.1007/s11666-007-9047-2.
[34] R. Hui et al., 'Thermal plasma spraying for SOFCs: Applications, potential advantages, and challenges', Journal of Power Sources, vol. 170, no. 2, pp. 308–323, Jul. 2007, doi: 10.1016/j.jpowsour.2007.03.075.
[35] D. R. Clarke, M. Oechsner, and N. P. Padture, 'Thermal-barrier coatings for more efficient gas-turbine engines', MRS Bulletin, vol. 37, no. 10, Art. no. 10, Oct. 2012, doi: 10.1557/mrs.2012.232.
[36] N. P. Padture, 'Thermal Barrier Coatings for Gas-Turbine Engine Applications', Science, vol. 296, no. 5566, Art. no. 5566, Apr. 2002, doi: 10.1126/science.1068609.
[37] V. Rat, C. Chazelas, S. Goutier, A. Keromnes, G. Mariaux, and A. Vardelle, 'In-Flight Mechanisms in Suspension Plasma Spraying: Issues and Perspectives', J Therm Spray Tech, vol. 31, no. 4, pp. 699–715, Apr. 2022, doi: 10.1007/s11666-022-01376-2.
[38] L. Łatka, 'Thermal Barrier Coatings Manufactured by Suspension Plasma Spraying - A Review', Advances in Materials Science, vol. 18, no. 3, pp. 95–117, Sep. 2018, doi: 10.1515/adms-2017-0044.
[39] P. Sokołowski, S. Kozerski, L. Pawłowski, and A. Ambroziak, 'The key process parameters influencing formation of columnar microstructure in suspension plasma sprayed zirconia coatings', Surface and Coatings Technology, vol. 260, pp. 97–106, Dec. 2014, doi: 10.1016/j.surfcoat.2014.08.078.

[40] F. Caio and C. Moreau, ‘Influence of Substrate Shape and Roughness on Coating Microstructure in Suspension Plasma Spray’, Coatings, vol. 9, no. 11, p. 746, Nov. 2019, doi: 10.3390/coatings9110746.
[41] K. VanEvery et al., ‘Column Formation in Suspension Plasma-Sprayed Coatings and Resultant Thermal Properties’, J Therm Spray Tech, vol. 20, no. 4, pp. 817–828, Jun. 2011, doi: 10.1007/s11666-011-9632-2.
[42] E. Aubignat et al., ‘Optimization of the injection with a twin-fluid atomizer for suspension plasma spray process using three non-intrusive diagnostic tools’, J Vis, vol. 19, no. 1, pp. 21–36, Feb. 2016, doi: 10.1007/s12650-015-0281-2.
[43] Y. Zhao et al., ‘Influence of Substrate Properties on the Formation of Suspension Plasma Sprayed Coatings’, J Therm Spray Tech, vol. 27, no. 1, pp. 73–83, Jan. 2018, doi: 10.1007/s11666-017-0671-1.
[44] A. Ganvir, R. F. Calinas, N. Markocsan, N. Curry, and S. Joshi, ‘Experimental visualization of microstructure evolution during suspension plasma spraying of thermal barrier coatings’, Journal of the European Ceramic Society, vol. 39, no. 2, pp. 470–481, Feb. 2019, doi: 10.1016/j.jeurceramsoc.2018.09.023.
[45] A. Joulia, W. Duarte, S. Goutier, M. Vardelle, A. Vardelle, and S. Rossignol, ‘Tailoring the Spray Conditions for Suspension Plasma Spraying’, J Therm Spray Tech, vol. 24, no. 1, Art. no. 1, Jan. 2015, doi: 10.1007/s11666-014-0184-0.
[46] B. Bernard et al., ‘Effect of Suspension Plasma-Sprayed YSZ Columnar Microstructure and Bond Coat Surface Preparation on Thermal Barrier Coating Properties’, J Therm Spray Tech, vol. 26, no. 6, pp. 1025–1037, Aug. 2017, doi: 10.1007/s11666-017-0584-z.
[47] N. Curry, Z. Tang, N. Markocsan, and P. Nylén, ‘Influence of bond coat surface roughness on the structure of axial suspension plasma spray thermal barrier coatings — Thermal and lifetime performance’, Surface and Coatings Technology, vol. 268, pp. 15–23, Apr. 2015, doi: 10.1016/j.surfcoat.2014.08.067.
[48] G. Bidron, S. Goutier, M. Vardelle, P. Denoirjean, and P. Fauchais, ‘Flattening behavior of micro- and nano-sized yttria-stabilized zirconia particles plasma-sprayed on smooth preheated (610 K) nickel substrate: part I’, J. Phys. D: Appl. Phys., vol. 52, no. 16, p. 165201, Feb. 2019, doi: 10.1088/1361-6463/aafd81.
[49] A. Dolmaire, S. Goutier, M. Vardelle, P.-M. Geffroy, and A. Joulia, ‘Investigations on Particle Behavior at the Stagnation Zone for a Suspension Particle Jet in Plasma Spray Conditions’, J Therm Spray Tech, vol. 30, no. 4, pp. 1001–1014, Apr. 2021, doi: 10.1007/s11666-021-01174-2.
[50] C. Delbos, J. Fazilleau, V. Rat, J. F. Coudert, P. Fauchais, and B. Pateyron, ‘Phenomena Involved in Suspension Plasma Spraying Part 2: Zirconia Particle Treatment and Coating Formation’, Plasma Chem Plasma Process, vol. 26, no. 4, pp. 393–414, Aug. 2006, doi: 10.1007/s11090-006-9020-8.
[51] J. Oberste-Berghaus, S. Bouaricha, J.-G. Legoux, and C. Moreau, ‘Injection conditions and in-flight particle states in suspension plasma spraying of alumina and zirconia nano-ceramics’, presented at the Proceedings of the Internation Thermal Spray Conference, Basel, 2005, pp. 2–4.
[52] R. Etchart-Salas et al., ‘Influence of Plasma Instabilities in Ceramic Suspension Plasma Spraying’, J Therm Spray Tech, vol. 16, no. 5, pp. 857–865, Dec. 2007, doi: 10.1007/s11666-007-9084-x.
[53] A. Dolmaire et al., ‘Benefits of Hydrogen in a Segmented-Anode Plasma Torch in Suspension Plasma Spraying’, J Therm Spray Tech, vol. 30, no. 1, pp. 236–250, Jan. 2021, doi: 10.1007/s11666-020-01134-2.
[54] R. Chidambaram Seshadri, G. Dwivedi, V. Viswanathan, and S. Sampath, ‘Characterizing Suspension Plasma Spray Coating Formation Dynamics through Curvature Measurements’, J Therm Spray Tech, vol. 25, no. 8, pp. 1666–1683, Dec. 2016, doi: 10.1007/s11666-016-0460-2.
[55] A. Ganvir, N. Curry, S. Björklund, N. Markocsan, and P. Nylén, ‘Characterization of Microstructure and Thermal Properties of YSZ Coatings Obtained by Axial Suspension Plasma Spraying (ASPS)’, J Therm Spray Tech, vol. 24, no. 7, pp. 1195–1204, Oct. 2015, doi: 10.1007/s11666-015-0263-x.

[56] X. Chen, S. Kuroda, T. Ohnuki, H. Araki, M. Watanabe, and Y. Sakka, 'Effects of Processing Parameters on the Deposition of Yttria Partially Stabilized Zirconia Coating During Suspension Plasma Spray', Journal of the American Ceramic Society, vol. 99, no. 11, pp. 3546–3555, 2016, doi: 10.1111/jace.14393.
[57] X. Chen et al., 'Highly Segmented Thermal Barrier Coatings Deposited by Suspension Plasma Spray: Effects of Spray Process on Microstructure', J Therm Spray Tech, vol. 25, no. 8, pp. 1638–1649, Dec. 2016, doi: 10.1007/s11666-016-0469-6.
[58] D. Zhou, O. Guillon, and R. Vaßen, 'Development of YSZ Thermal Barrier Coatings Using Axial Suspension Plasma Spraying', Coatings, vol. 7, no. 8, p. 120, Aug. 2017, doi: 10.3390/coatings7080120.
[59] P. Fauchais, R. Etchart-Salas, V. Rat, J. F. Coudert, N. Caron, and K. Wittmann-Ténèze, 'Parameters Controlling Liquid Plasma Spraying: Solutions, Sols, or Suspensions', Journal of Thermal Spray Technology, vol. 17, no. 1, pp. 31–59, Mar. 2008, doi: 10.1007/s11666-007-9152-2.
[60] M. Jadidi, M. Mousavi, S. Moghtadernejad, and A. Dolatabadi, 'A Three-Dimensional Analysis of the Suspension Plasma Spray Impinging on a Flat Substrate', J Therm Spray Tech, vol. 24, no. 1, pp. 11–23, Jan. 2015, doi: 10.1007/s11666-014-0166-2.
[61] C. G. Phillips and S. R. Kaye, 'THE INFLUENCE OF THE VISCOUS BOUNDARY LAYER ON THE CRITICAL STOKES NUMBER FOR PARTICLE IMPACTION NEAR A STAGNATION POINT', Journal of Aerosol Science, vol. 30, no. 6, pp. 709–718, Jul. 1999, doi: 10.1016/S0021-8502(98)00766-6.
[62] A. Farrokhpanah, T. W. Coyle, and J. Mostaghimi, 'Numerical Study of Suspension Plasma Spraying', J Therm Spray Tech, vol. 26, no. 1, pp. 12–36, Jan. 2017, doi: 10.1007/s11666-016-0502-9.
[63] K. Pourang, C. Moreau, and A. Dolatabadi, 'Effect of Substrate and Its Shape on in-Flight Particle Characteristics in Suspension Plasma Spraying', J Therm Spray Tech, vol. 25, no. 1, Art. no. 1, Jan. 2016, doi: 10.1007/s11666-015-0342-z.
[64] B. Bernard, 'Barrières thermiques par projection plasma de suspensions : développement et caractérisation de microstructures à faible conductivité thermique', Université de Lorraine, 2016.
[65] J. Joeris, A. Tiwari, S. Brinckmann, F. Kurze, O. Guillon, and R. Vaßen, 'Evaluation of major factors influencing the TBC topcoat formation in axial suspension plasma spraying (SPS)', International Journal of Applied Ceramic Technology, doi: 10.1111/ijac.14288.
[66] Y. Zhao et al., 'Thermal shock behaviors of YSZ thick thermal barrier coatings fabricated by suspension and atmospheric plasma spraying', Surface and Coatings Technology, vol. 249, pp. 48–55, Jun. 2014, doi: 10.1016/j.surfcoat.2014.03.046.
[67] N. Curry, K. VanEvery, T. Snyder, and N. Markocsan, 'Thermal Conductivity Analysis and Lifetime Testing of Suspension Plasma-Sprayed Thermal Barrier Coatings', Coatings, vol. 4, no. 3, pp. 630–650, Sep. 2014, doi: 10.3390/coatings4030630.
[68] M. Gupta, N. Markocsan, X.-H. Li, and B. Kjellman, 'Development of bondcoats for high lifetime suspension plasma sprayed thermal barrier coatings', Surface and Coatings Technology, vol. 371, pp. 366–377, Aug. 2019, doi: 10.1016/j.surfcoat.2018.11.013.
[69] S. Mahade et al., 'Understanding the effect of material composition and microstructural design on the erosion behavior of plasma sprayed thermal barrier coatings', Applied Surface Science, vol. 488, pp. 170–184, Sep. 2019, doi: 10.1016/j.apsusc.2019.05.245.
[70] R. S. Lima, B. M. H. Guerreiro, and M. Aghasibeig, 'Microstructural Characterization and Room-Temperature Erosion Behavior of As-Deposited SPS, EB-PVD and APS YSZ-Based TBCs', J Therm Spray Tech, vol. 28, no. 1, pp. 223–232, Jan. 2019, doi: 10.1007/s11666-018-0763-6.
[71] B. Bernard et al., 'Thermal insulation properties of YSZ coatings: Suspension Plasma Spraying (SPS) versus Electron Beam Physical Vapor Deposition (EB-PVD) and Atmospheric Plasma Spraying (APS)', Surface and Coatings Technology, Jun. 2016, doi: 10.1016/j.surfcoat.2016.06.010.
[72] A. Ganvir, N. Curry, S. Govindarajan, and N. Markocsan, 'Characterization of Thermal Barrier Coatings Produced by Various Thermal Spray Techniques Using Solid Powder, Suspension, and

Solution Precursor Feedstock Material', International Journal of Applied Ceramic Technology, vol. 13, no. 2, pp. 324–332, 2016, doi: 10.1111/ijac.12472.
[73] P. Su-ungkavatin, L. Tiruta-Barna, and L. Hamelin, 'Biofuels, electrofuels, electric or hydrogen?: A review of current and emerging sustainable aviation systems', Progress in Energy and Combustion Science, vol. 96, p. 101073, May 2023, doi: 10.1016/j.pecs.2023.101073.
[74] E. Cabrera and J. M. M. de Sousa, 'Use of Sustainable Fuels in Aviation—A Review', Energies, vol. 15, no. 7, Art. no. 7, Jan. 2022, doi: 10.3390/en15072440.
[75] C. Irimiea et al., 'ALTERNATE: Experimental and modeling study of soot formation in high-pressure kerosene and SAF combustion', presented at the Towards Sustainable Aviation Summit 2022 (TSAS 2022), Oct. 2022. Accessed: Mar. 01, 2023. [Online]. Available: https://hal.science/hal-03943930
[76] W. R. Chen and L. R. Zhao, 'Review – Volcanic Ash and its Influence on Aircraft Engine Components', Procedia Engineering, vol. 99, pp. 795–803, 2015, doi: 10.1016/j.proeng.2014.12.604.
[77] R. V. Martin, 'Satellite remote sensing of surface air quality', Atmospheric Environment, vol. 42, no. 34, pp. 7823–7843, Nov. 2008, doi: 10.1016/j.atmosenv.2008.07.018.
[78] R. M. Hoff and S. A. Christopher, 'Remote Sensing of Particulate Pollution from Space: Have We Reached the Promised Land?', Journal of the Air & Waste Management Association, vol. 59, no. 6, pp. 645–675, Jun. 2009, doi: 10.3155/1047-3289.59.6.645.
[79] 'Ambient (outdoor) air pollution'. https://www.who.int/news-room/fact-sheets/detail/ambient-(outdoor)-air-quality-and-health (accessed Feb. 22, 2023).
[80] A. Nieto, R. Agrawal, L. Bravo, C. Hofmeister-Mock, M. Pepi, and A. Ghoshal, 'Calcia–magnesia–alumina–silicate (CMAS) attack mechanisms and roadmap towards Sandphobic thermal and environmental barrier coatings', International Materials Reviews, vol. 66, no. 7, pp. 451–492, Oct. 2021, doi: 10.1080/09506608.2020.1824414.
[81] D. A. van et al., 'Global Estimates of Ambient Fine Particulate Matter Concentrations from Satellite-Based Aerosol Optical Depth: Development and Application', Environmental Health Perspectives, vol. 118, no. 6, pp. 847–855, Jun. 2010, doi: 10.1289/ehp.0901623.
[82] F. Amato et al., 'Concentrations, sources and geochemistry of airborne particulate matter at a major European airport', Journal of Environmental Monitoring, vol. 12, no. 4, pp. 854–862, 2010, doi: 10.1039/B925439K.
[83] A. Shahsavani et al., 'The evaluation of PM10, PM2.5, and PM1 concentrations during the Middle Eastern Dust (MED) events in Ahvaz, Iran, from april through september 2010', Journal of Arid Environments, vol. 77, pp. 72–83, Feb. 2012, doi: 10.1016/j.jaridenv.2011.09.007.
[84] J. Amanollahi, S. Kaboodvandpour, A. M. Abdullah, and M. F. Ramli, 'Accuracy assessment of moderate resolution image spectroradiometer products for dust storms in semiarid environment', Int. J. Environ. Sci. Technol., vol. 8, no. 2, pp. 373–380, Mar. 2011, doi: 10.1007/BF03326224.
[85] A. Altuwayjiri, M. Pirhadi, M. Kalafy, B. Alharbi, and C. Sioutas, 'Impact of different sources on the oxidative potential of ambient particulate matter PM10 in Riyadh, Saudi Arabia: A focus on dust emissions', Science of The Total Environment, Feb. 2022, doi: 10.1016/j.scitotenv.2021.150590.
[86] A. Amarloei, M. Fazlzadeh, A. J. Jafari, A. Zarei, and S. Mazloomi, 'Particulate matters and bioaerosols during Middle East dust storms events in Ilam, Iran', Microchemical Journal, vol. 152, p. 104280, Jan. 2020, doi: 10.1016/j.microc.2019.104280.
[87] V. Tsiouri, K. E. Kakosimos, and P. Kumar, 'Concentrations, sources and exposure risks associated with particulate matter in the Middle East Area—a review', Air Qual Atmos Health, vol. 8, no. 1, pp. 67–80, Feb. 2015, doi: 10.1007/s11869-014-0277-4.
[88] N. A. Saliba, F. El Jam, G. El Tayar, W. Obeid, and M. Roumie, 'Origin and variability of particulate matter (PM10 and PM2.5) mass concentrations over an Eastern Mediterranean city', Atmospheric Research, vol. 97, no. 1, pp. 106–114, Jul. 2010, doi: 10.1016/j.atmosres.2010.03.011.
[89] A. Al-Zu'bi, 'Evaluation of the Jordanian environmental legislations.', World Applied Sciences Journal, vol. 14, no. 10, pp. 1438–1444, 2011.

[90] E. Al Katheeri, F. Al Jallad, and M. Al Omar, ‘Assessment of gaseous and particulate pollutants in the ambient air in Al Mirfa City, United Arab Emirates’, Journal of Environmental Protection, vol. 3, no. 7, pp. 640–7, 2012.
[91] D. Alexander, ‘Volcanic ash in the atmosphere and risks for civil aviation: A study in European crisis management’, Int J Disaster Risk Sci, vol. 4, no. 1, pp. 9–19, Mar. 2013, doi: 10.1007/s13753-013-0003-0.
[92] T. Bolić and Ź. Sivčev, ‘Eruption of Eyjafjallajökull in Iceland: Experience of European Air Traffic Management’, Transportation Research Record, vol. 2214, no. 1, pp. 136–143, Jan. 2011, doi: 10.3141/2214-17.
[93] M. Mazzocchi, F. Hansstein, and M. Ragona, ‘The 2010 volcanic ash cloud and its financial impact on the European airline industry’, in CESifo Forum, München: ifo Institut für Wirtschaftsforschung an der Universität München, 2010, pp. 92–100.
[94] M. Ragona, F. Hannstein, and M. Mazzocchi, ‘The financial impact of the volcanic ash crisis on the European airline industry’, Governing Disasters: The Challenges of Emergency Risk Regulafion, pp. 27–50, 2011.
[95] S. Elgobashi, ‘An updated classification map of particle-laden turbulent flows’, in IUTAM Symposium on Computational Approaches to Multiphase Flow, Springer, 2006, pp. 3–10.
[96] S. Elghobashi, ‘On predicting particle-laden turbulent flows’, Appl. Sci. Res., vol. 52, no. 4, pp. 309–329, Jun. 1994, doi: 10.1007/BF00936835.
[97] N. Bojdo, A. Filippone, B. Parkes, and R. Clarkson, ‘Aircraft engine dust ingestion following sand storms’, Aerospace Science and Technology, vol. 106, p. 106072, Nov. 2020, doi: 10.1016/j.ast.2020.106072.
[98] N. Bojdo, ‘Rotorcraft Engine Air Particle Separation’, University of Manchester, 2013.
[99] N. Bojdo, M. Ellis, A. Filippone, M. Jones, and A. Pawley, ‘Particle-Vane Interaction Probability in Gas Turbine Engines’, Journal of Turbomachinery, vol. 141, no. 9, Jun. 2019, doi: 10.1115/1.4043953.
[100] N. Bojdo and A. Filippone, ‘A Simple Model to Assess the Role of Dust Composition and Size on Deposition in Rotorcraft Engines’, Aerospace, vol. 6, no. 4, Art. no. 4, Apr. 2019, doi: 10.3390/aerospace6040044.
[101] M. Ellis, N. Bojdo, A. Filippone, and R. Clarkson, ‘Monte Carlo Predictions of Aero-Engine Performance Degradation Due to Particle Ingestion’, Aerospace, vol. 8, no. 6, Art. no. 6, Jun. 2021, doi: 10.3390/aerospace8060146.
[102] S. Abdelouhab, R. Podor, C. Rapin, M. J. Toplis, P. Berthod, and M. Vilasi, ‘Determination of Na2O activities in silicate melts by EMF measurements’, Journal of Non-Crystalline Solids, vol. 354, no. 26, Art. no. 26, May 2008, doi: 10.1016/j.jnoncrysol.2007.12.003.
[103] M. Craig, N. L. Ndamka, R. G. Wellman, and J. R. Nicholls, ‘CMAS degradation of EB-PVD TBCs: The effect of basicity’, Surface and Coatings Technology, vol. 270, pp. 145–153, May 2015, doi: 10.1016/j.surfcoat.2015.03.009.
[104] J. Phalippou, ‘Verres: aspects théoriques’, Techniques de l’ingénieur. Sciences fondamentales, vol. 7, no. AF3600, pp. AF3600-1, 2001.
[105] Y. Wu et al., ‘Comparison of CMAS corrosion and sintering induced microstructural characteristics of APS thermal barrier coatings’, Journal of Materials Science & Technology, vol. 35, no. 3, pp. 440–447, Mar. 2019, doi: 10.1016/j.jmst.2018.09.046.
[106] D. Ghosh and A. Chatterjee, Iron making and steelmaking: Theory and Practice. PHI Learning Pvt. Ltd., 2008.
[107] C. Petitjean, P.-J. Panteix, C. Rapin, M. Vilasi, and R. Podor, ‘Electrochemical behavior of glass melts: application to corrosion processes’, in 2nd International summer school on nuclear glass wasteform: Structure, Properties , and long-term behavior (SUMGLASS 2013), Angeli, F, Delaye, JM, Schuller, S, Pinet, O, Rebiscoul, D, Gin, S, Peuget, and S, Eds., in Procedia Materials Science, vol. 7. 2014, pp. 101–110. doi: 10.1016/j.mspro.2014.10.014.
[108] N. Chellah, M. H. Vidal-Setif, C. Petitjean, P. J. Panteix, C. Rapin, and M. Vilasi, ‘Calcium-Magnesium-Alumino-Silicate (CMAS) degradation of thermal barrier coatings: solubility of different oxides from ZrO2-Nd2O3 system in a model CMAS’, presented at the HTCPM8, Les Embiez, May 2012.
[109] C. Bodsworth, ‘HBB’, Physical Chemistry of Iron and Steel Manufacture, 1972.

[110] R. W. Jackson, E. M. Zaleski, D. L. Poerschke, B. T. Hazel, M. R. Begley, and C. G. Levi, 'Interaction of molten silicates with thermal barrier coatings under temperature gradients', Acta Materialia, vol. 89, pp. 396–407, May 2015, doi: 10.1016/j.actamat.2015.01.038.
[111] J. P. Engelbrecht, E. V. McDonald, J. A. Gillies, R. K. M. Jayanty, G. Casuccio, and A. W. Gertler, 'Characterizing Mineral Dusts and Other Aerosols from the Middle East—Part 1: Ambient Sampling', Inhalation Toxicology, vol. 21, no. 4, pp. 297–326, Apr. 2009, doi: 10.1080/08958370802464273.
[112] A. Aygun, A. L. Vasiliev, N. P. Padture, and X. Ma, 'Novel thermal barrier coatings that are resistant to high-temperature attack by glassy deposits', Acta Materialia, vol. 55, no. 20, Art. no. 20, Dec. 2007, doi: 10.1016/j.actamat.2007.08.028.
[113] M. P. Borom, C. A. Johnson, and L. A. Peluso, 'Role of environment deposits and operating surface temperature in spallation of air plasma sprayed thermal barrier coatings', Surface and Coatings Technology, vol. 86, pp. 116–126, 1996.
[114] S. Krämer, J. Yang, C. G. Levi, and C. A. Johnson, 'Thermochemical Interaction of Thermal Barrier Coatings with Molten CaO-MgO-Al2O3-SiO2 (CMAS) Deposits', Journal of the American Ceramic Society, vol. 89, no. 10, Art. no. 10, Oct. 2006, doi: 10.1111/j.1551-2916.2006.01209.x.
[115] S. Morelli et al., 'CMAS corrosion of YSZ thermal barrier coatings obtained by different thermal spray processes', Journal of the European Ceramic Society, vol. 40, no. 12, pp. 4084–4100, Sep. 2020, doi: 10.1016/j.jeurceramsoc.2020.04.058.
[116] R. Wellman, G. Whitman, and J. R. Nicholls, 'CMAS corrosion of EB PVD TBCs: Identifying the minimum level to initiate damage', International Journal of Refractory Metals and Hard Materials, vol. 28, no. 1, Art. no. 1, Jan. 2010, doi: 10.1016/j.ijrmhm.2009.07.005.
[117] M. H. Vidal-Sétif, C. Rio, D. Boivin, and O. Lavigne, 'Microstructural characterization of the interaction between 8YPSZ (EB-PVD) thermal barrier coatings and a synthetic CAS', Surface and Coatings Technology, vol. 239, pp. 41–48, Jan. 2014, doi: 10.1016/j.surfcoat.2013.11.014.
[118] B. M. Wilke, B. J. Duke, and W. L. O. Jimoh, 'Mineralogy and chemistry of harmattan dust in Northern Nigeria', CATENA, vol. 11, no. 1, pp. 91–96, Jan. 1984, doi: 10.1016/S0341-8162(84)80009-0.
[119] A. S. Goudie, 'Dust storms and their geomorphological implications', Journal of Arid Environments, vol. 1, no. 4, pp. 291–311, Dec. 1978, doi: 10.1016/S0140-1963(18)31712-9.
[120] H. E. Taylor and F. E. Lichte, 'Chemical composition of Mount St. Helens volcanic ash', Geophysical Research Letters, vol. 7, no. 11, pp. 949–952, 1980, doi: 10.1029/GL007i011p00949.
[121] A. K. Rai, R. S. Bhattacharya, D. E. Wolfe, and T. J. Eden, 'CMAS-Resistant Thermal Barrier Coatings (TBC): CMAS-Resistant Thermal Barrier Coatings', International Journal of Applied Ceramic Technology, vol. 7, no. 5, Art. no. 5, May 2009, doi: 10.1111/j.1744-7402.2009.02373.x.
[122] W. Braue, 'Environmental stability of the YSZ layer and the YSZ/TGO interface of an in-service EB-PVD coated high-pressure turbine blade', J Mater Sci, vol. 44, no. 7, pp. 1664–1675, Apr. 2009, doi: 10.1007/s10853-008-3215-8.
[123] H. Fang et al., 'Comparative study on failure behavior of promising CMAS-resistant plasma-sprayed thermal barrier coatings in burner rig test with/without CMAS deposition', Ceramics International, Dec. 2022, doi: 10.1016/j.ceramint.2022.12.099.
[124] N. L. Ndamka, R. G. Wellman, and J. R. Nicholls, 'The degradation of thermal barrier coatings by molten deposits: introducing the concept of basicity', Materials at High Temperatures, vol. 33, no. 1, Art. no. 1, Jan. 2016, doi: 10.1179/1878641315Y.0000000017.
[125] F. Perrudin, 'Étude de la dissolution de diverses terres rares dans des liquides silicatés (CMAS) de composition variable : contribution au développement des barrières thermiques en ZRO_2-RE_2O_3 (RE=La-Lu)', Université de Lorraine, 2018.
[126] F. H. Stott, D. J. De Wet, and R. Taylor, 'Degradation of Thermal-Barrier Coatings at Very High Temperatures.', MRS Bulletin, vol. 19, no. 10, Art. no. 10, 1994.
[127] P. Svancarek et al., 'A comparison of the microstructure and mechanical properties of two liquid phase sintered aluminas containing different molar ratios of calcia–silica sintering additives',

Journal of the European Ceramic Society, vol. 24, no. 12, pp. 3453–3463, Jan. 2004, doi: 10.1016/j.jeurceramsoc.2003.10.032.
[128] D. L. Poerschke, T. L. Barth, and C. G. Levi, 'Equilibrium relationships between thermal barrier oxides and silicate melts', Acta Materialia, vol. 120, pp. 302–314, 2016, doi: https://doi.org/10.1016/j.actamat.2016.08.077.
[129] D. L. Poerschke, R. W. Jackson, and C. G. Levi, 'Silicate Deposit Degradation of Engineered Coatings in Gas Turbines: Progress Toward Models and Materials Solutions', Annu. Rev. Mater. Res., vol. 47, no. 1, Art. no. 1, Jul. 2017, doi: 10.1146/annurev-matsci-010917-105000.
[130] F. Perrudin, M. H. Vidal-Sétif, C. Rio, C. Petitjean, P. J. Panteix, and M. Vilasi, 'Influence of rare earth oxides on kinetics and reaction mechanisms in CMAS silicate melts', Journal of the European Ceramic Society, vol. 39, no. 14, Art. no. 14, Nov. 2019, doi: 10.1016/j.jeurceramsoc.2019.06.036.
[131] C. G. Levi, J. W. Hutchinson, M.-H. Vidal-Sétif, and C. A. Johnson, 'Environmental degradation of thermal-barrier coatings by molten deposits', MRS Bulletin, vol. 37, no. 10, Art. no. 10, Oct. 2012, doi: 10.1557/mrs.2012.230.
[132] C. Mercer, S. Faulhaber, A. G. Evans, and R. Darolia, 'A delamination mechanism for thermal barrier coatings subject to calcium–magnesium–alumino-silicate (CMAS) infiltration', Acta Materialia, vol. 53, no. 4, Art. no. 4, Feb. 2005, doi: 10.1016/j.actamat.2004.11.028.
[133] X. Chen, 'Calcium–magnesium–alumina–silicate (CMAS) delamination mechanisms in EB-PVD thermal barrier coatings', Surface and Coatings Technology, vol. 200, no. 11, pp. 3418–3427, Mar. 2006, doi: 10.1016/j.surfcoat.2004.12.029.
[134] A. G. Evans and J. W. Hutchinson, 'The mechanics of coating delamination in thermal gradients', Surface and Coatings Technology, vol. 201, no. 18, pp. 7905–7916, Jun. 2007, doi: 10.1016/j.surfcoat.2007.03.029.
[135] A. Vogel, R. Clarkson, A. Durant, M. Cassiani, and A. Stohl, 'Volcanic ash ingestion by a large gas turbine aeroengine: fan-particle interaction', pp. EPSC2016-15419, Apr. 2016.
[136] C. Taltavull, J. Dean, and T. W. Clyne, 'Adhesion of Volcanic Ash Particles under Controlled Conditions and Implications for Their Deposition in Gas Turbines', Advanced Engineering Materials, vol. 18, no. 5, pp. 803–813, 2016, doi: 10.1002/adem.201500371.
[137] C. S. Holgate, G. G. E. Seward, A. R. Ericks, D. L. Poerschke, and C. G. Levi, 'Dissolution and diffusion kinetics of yttria-stabilized zirconia into molten silicates', Journal of the European Ceramic Society, vol. 41, no. 3, pp. 1984–1994, Mar. 2021, doi: 10.1016/j.jeurceramsoc.2020.10.056.
[138] T. Strangman, D. Raybould, A. Jameel, and W. Baker, 'Damage mechanisms, life prediction, and development of EB-PVD thermal barrier coatings for turbine airfoils', Surface and Coatings Technology, vol. 202, no. 4–7, Art. no. 4–7, Dec. 2007, doi: 10.1016/j.surfcoat.2007.06.067.
[139] J. R. VanValzah and H. E. Eaton, 'Cooling rate effects on the tetragonal to monoclinic phase transformation in aged plasma-sprayed yttria partially stabilized zirconia', Surface and Coatings Technology, vol. 46, no. 3, Art. no. 3, Sep. 1991, doi: 10.1016/0257-8972(91)90171-R.
[140] S. Krämer et al., 'Mechanisms of cracking and delamination within thick thermal barrier systems in aero-engines subject to calcium-magnesium-alumino-silicate (CMAS) penetration', Materials Science and Engineering: A, vol. 490, no. 1–2, Art. no. 1–2, Aug. 2008, doi: 10.1016/j.msea.2008.01.006.
[141] M. H. Vidal-Setif, N. Chellah, C. Rio, C. Sanchez, and O. Lavigne, 'Calcium–magnesium–alumino-silicate (CMAS) degradation of EB-PVD thermal barrier coatings: Characterization of CMAS damage on ex-service high pressure blade TBCs', Surface and Coatings Technology, vol. 208, pp. 39–45, Sep. 2012, doi: 10.1016/j.surfcoat.2012.07.074.
[142] A. D. Gledhill, K. M. Reddy, J. M. Drexler, K. Shinoda, S. Sampath, and N. P. Padture, 'Mitigation of damage from molten fly ash to air-plasma-sprayed thermal barrier coatings', Materials Science and Engineering: A, vol. 528, no. 24, Art. no. 24, Sep. 2011, doi: 10.1016/j.msea.2011.06.041.
[143] F. H. Stott, R. Taylor, and D. J. de Wet, 'The effects of molten silicate deposits on the stability of thermal barrier coatings for turbine applications at very high temperatures', in Proceedings of advanced materials, 1992.

[144] A. R. Krause, H. F. Garces, G. Dwivedi, A. L. Ortiz, S. Sampath, and N. P. Padture, 'Calcia-magnesia-alumino-silicate (CMAS)-induced degradation and failure of air plasma sprayed yttria-stabilized zirconia thermal barrier coatings', Acta Materialia, vol. 105, pp. 355–366, Feb. 2016, doi: 10.1016/j.actamat.2015.12.044.
[145] J. Kim, M. G. Dunn, A. J. Baran, D. P. Wade, and E. L. Tremba, 'Deposition of Volcanic Materials in the Hot Sections of Two Gas Turbine Engines', Journal of Engineering for Gas Turbines and Power, vol. 115, no. 3, pp. 641–651, Jul. 1993, doi: 10.1115/1.2906754.
[146] F. Döring, S. Staudacher, C. Koch, and M. Weißschuh, 'Modeling Particle Deposition Effects in Aircraft Engine Compressors', Journal of Turbomachinery, vol. 139, no. 5, Jan. 2017, doi: 10.1115/1.4035072.
[147] R. Clarkson and H. Simpson, 'Maximising airspace use during volcanic eruptions: matching engine durability against ash cloud occurrence', in Proceedings of the NATO STO AVT-272 Specialists Meeting on: Impact of Volcanic Ash Clouds on Military Operations, Vilnius, Lithuania, 2017, pp. 15–17.
[148] R. J. Clarkson, E. J. Majewicz, and P. Mack, 'A re-evaluation of the 2010 quantitative understanding of the effects volcanic ash has on gas turbine engines', Proceedings of the Institution of Mechanical Engineers, Part G: Journal of Aerospace Engineering, vol. 230, no. 12, pp. 2274–2291, Oct. 2016, doi: 10.1177/0954410015623372.
[149] D. Li, P. Jiang, R. Gao, F. Sun, X. Jin, and X. Fan, 'Experimental and numerical investigation on the thermal and mechanical behaviours of thermal barrier coatings exposed to CMAS corrosion', J Adv Ceram, vol. 10, no. 3, pp. 551–564, Jun. 2021, doi: 10.1007/s40145-021-0457-2.
[150] X. Shan et al., 'Buckling failure in air-plasma sprayed thermal barrier coatings induced by molten silicate attack', Scripta Materialia, vol. 113, pp. 71–74, Mar. 2016, doi: 10.1016/j.scriptamat.2015.09.029.
[151] X. Chen, R. Wang, N. Yao, A. G. Evans, J. W. Hutchinson, and R. W. Bruce, 'Foreign object damage in a thermal barrier system: mechanisms and simulations', Materials Science and Engineering: A, vol. 352, no. 1–2, Art. no. 1–2, Jul. 2003, doi: 10.1016/S0921-5093(02)00905-X.
[152] G. Zhang, X. Fan, R. Xu, L. Su, and T. J. Wang, 'Transient thermal stress due to the penetration of calcium-magnesium-alumino-silicate in EB-PVD thermal barrier coating system', Ceramics International, vol. 44, no. 11, pp. 12655–12663, Aug. 2018, doi: 10.1016/j.ceramint.2018.04.065.
[153] H. Peng, L. Wang, L. Guo, W. Miao, H. Guo, and S. Gong, 'Degradation of EB-PVD thermal barrier coatings caused by CMAS deposits', Progress in Natural Science: Materials International, vol. 22, no. 5, Art. no. 5, Oct. 2012, doi: 10.1016/j.pnsc.2012.06.007.
[154] L. Guo, G. Li, and Z. Gan, 'Effects of surface roughness on CMAS corrosion behavior for thermal barrier coating applications', J Adv Ceram, vol. 10, no. 3, pp. 472–481, Jun. 2021, doi: 10.1007/s40145-020-0449-7.
[155] N. L. Ndamka, 'Microstructural damage of thermal barrier coatings due to CMAS', Cranfield University, 2013.
[156] S. Mahade, N. Curry, S. Björklund, N. Markocsan, and P. Nylén, 'Failure analysis of Gd2Zr2O7/YSZ multi-layered thermal barrier coatings subjected to thermal cyclic fatigue', Journal of Alloys and Compounds, vol. 689, pp. 1011–1019, Dec. 2016, doi: 10.1016/j.jallcom.2016.07.333.
[157] A. G. Evans, D. R. Mumm, J. W. Hutchinson, G. H. Meier, and F. S. Pettit, 'Mechanisms controlling the durability of thermal barrier coatings', Progress in materials science, vol. 46, no. 5, Art. no. 5, 2001.
[158] S. Dryepondt, J. R. Porter, and D. R. Clarke, 'On the initiation of cyclic oxidation-induced rumpling of platinum-modified nickel aluminide coatings', Acta Materialia, vol. 57, no. 6, pp. 1717–1723, Apr. 2009, doi: 10.1016/j.actamat.2008.12.015.
[159] I. T. Spitsberg, D. R. Mumm, and A. G. Evans, 'On the failure mechanisms of thermal barrier coatings with diffusion aluminide bond coatings', Materials Science and Engineering: A, vol. 394, no. 1, pp. 176–191, Mar. 2005, doi: 10.1016/j.msea.2004.11.038.

[160] V. K. Tolpygo and D. R. Clarke, ‘Surface rumpling of a (Ni, Pt)Al bond coat induced by cyclic oxidation’, Acta Materialia, vol. 48, no. 13, pp. 3283–3293, Aug. 2000, doi: 10.1016/S1359-6454(00)00156-7.
[161] J. A. Ruud, A. Bartz, M. P. Borom, and C. A. Johnson, ‘Strength Degradation and Failure Mechanisms of Electron-Beam Physical-Vapor-Deposited Thermal Barrier Coatings’, Journal of the American Ceramic Society, vol. 84, no. 7, pp. 1545–1552, 2001, doi: 10.1111/j.1151-2916.2001.tb00875.x.
[162] C. S. Giggins, B. H. Kear, F. S. Pettit, and J. K. Tien, ‘Factors affecting adhesion of oxide scales on alloys’, Metall Trans B, vol. 5, no. 7, pp. 1685–1688, Jul. 1974, doi: 10.1007/BF02646343.
[163] H. E. Evans, ‘Modelling oxide spallation’, Materials at High Temperatures, vol. 12, no. 2–3, pp. 219–227, Jun. 1994, doi: 10.1080/09603409.1994.11689489.
[164] V. K. Tolpygo and D. R. Clarke, ‘On the rumpling mechanism in nickel-aluminide coatings: Part II: characterization of surface undulations and bond coat swelling’, Acta Materialia, vol. 52, no. 17, pp. 5129–5141, Oct. 2004, doi: 10.1016/j.actamat.2004.07.023.
[165] V. K. Tolpygo, D. R. Clarke, and K. S. Murphy, ‘Oxidation-induced failure of EB-PVD thermal barrier coatings’, Surface and Coatings Technology, vol. 146–147, pp. 124–131, Sep. 2001, doi: 10.1016/S0257-8972(01)01482-7.
[166] H. Zhao, Z. Yu, and H. N. G. Wadley, ‘The influence of coating compliance on the delamination of thermal barrier coatings’, Surface and Coatings Technology, vol. 204, no. 15, pp. 2432–2441, Apr. 2010, doi: 10.1016/j.surfcoat.2010.01.018.
[167] H. Dong, G.-J. Yang, H.-N. Cai, H. Ding, C.-X. Li, and C.-J. Li, ‘The influence of temperature gradient across YSZ on thermal cyclic lifetime of plasma-sprayed thermal barrier coatings’, Ceramics International, vol. 41, no. 9, Part A, pp. 11046–11056, Nov. 2015, doi: 10.1016/j.ceramint.2015.05.049.
[168] D. Zhu and R. A. Miller, ‘Determination of creep behavior of thermal barrier coatings under laser imposed high thermal and stress gradient conditions’, Journal of Materials Research, vol. 14, no. 1, pp. 146–161, Jan. 1999, doi: 10.1557/JMR.1999.0023.
[169] R. Vaßen, Y. Kagawa, R. Subramanian, P. Zombo, and D. Zhu, ‘Testing and evaluation of thermal-barrier coatings’, MRS Bulletin, vol. 37, no. 10, pp. 911–916, Oct. 2012, doi: 10.1557/mrs.2012.235.
[170] R. Musalek, T. Tesar, J. Medricky, F. Lukac, and R. S. Lima, ‘High-Temperature Cycling of Plasma Sprayed Multilayered NiCrAlY/YSZ/GZO/YAG Thermal Barrier Coatings Prepared from Liquid Feedstocks’, J Therm Spray Tech, vol. 30, no. 1, pp. 81–96, Jan. 2021, doi: 10.1007/s11666-020-01107-5.
[171] D. Zhu and R. A. Miller, ‘Thermal conductivity and elastic modulus evolution of thermal barrier coatings under high heat flux conditions’, J Therm Spray Tech, vol. 9, no. 2, pp. 175–180, Jun. 2000, doi: 10.1361/105996300770349890.
[172] D. Nies, R. Pulz, S. Glaubitz, M. Finn, B. Rehmer, and B. Skrotzki, ‘Testing of Thermal Barrier Coatings by Laser Excitation’, Advanced Engineering Materials, vol. 12, no. 12, pp. 1224–1229, 2010, doi: 10.1002/adem.201000212.
[173] Y. Wu et al., ‘Laser Thermal Gradient Testing and Fracture Mechanics Study of a Thermal Barrier Coating’, J Therm Spray Tech, vol. 28, no. 6, pp. 1239–1251, Aug. 2019, doi: 10.1007/s11666-019-00879-9.
[174] M. M. Gentleman, J. I. Eldridge, D. M. Zhu, K. S. Murphy, and D. R. Clarke, ‘Non-contact sensing of TBC/BC interface temperature in a thermal gradient’, Surface and Coatings Technology, vol. 201, no. 7, pp. 3937–3941, Dec. 2006, doi: 10.1016/j.surfcoat.2006.08.102.
[175] R. W. Jackson, E. M. Zaleski, B. T. Hazel, M. R. Begley, and C. G. Levi, ‘Response of molten silicate infiltrated Gd2Zr2O7 thermal barrier coatings to temperature gradients’, Acta Materialia, vol. 132, pp. 538–549, Jun. 2017, doi: 10.1016/j.actamat.2017.03.081.
[176] L. Yang, Y. C. Zhou, W. G. Mao, and C. Lu, ‘Real-time acoustic emission testing based on wavelet transform for the failure process of thermal barrier coatings’, Applied Physics Letters, vol. 93, no. 23, p. 231906, Dec. 2008, doi: 10.1063/1.3043458.
[177] H. Wang and R. B. Dinwiddie, ‘Characterization of Thermal Barrier Coatings Using Thermal Methods’, Advanced Engineering Materials, vol. 3, no. 7, pp. 465–468, 2001, doi: 10.1002/1527-2648(200107)3:7<465::AID-ADEM465>3.0.CO;2-G.

[178] J. Voyer, F. Gitzhofer, and M. I. Boulos, ‘Study of the performance of TBC under thermal cycling conditions using an acoustic emission rig’, J Therm Spray Tech, vol. 7, no. 2, pp. 181–190, Jun. 1998, doi: 10.1361/105996398770350909.
[179] F. Traeger, R. Vaßen, K.-H. Rauwald, and D. Stöver, ‘Thermal Cycling Setup for Testing Thermal Barrier Coatings’, Advanced Engineering Materials, vol. 5, no. 6, pp. 429–432, 2003, doi: 10.1002/adem.200300337.
[180] W. Zhu, Z. Y. Li, L. Yang, Y. C. Zhou, and J. F. Wei, ‘Real-time Detection of CMAS Corrosion Failure in APS Thermal Barrier Coatings Under Thermal Shock’, Exp Mech, vol. 60, no. 6, pp. 775–785, Jul. 2020, doi: 10.1007/s11340-020-00603-7.
[181] T. Steinke, D. Sebold, D. E. Mack, R. Vaßen, and D. Stöver, ‘A novel test approach for plasma-sprayed coatings tested simultaneously under CMAS and thermal gradient cycling conditions’, Surface and Coatings Technology, vol. 205, no. 7, pp. 2287–2295, Dec. 2010, doi: 10.1016/j.surfcoat.2010.09.008.
[182] D. S. Fox, R. A. Miller, D. Zhu, M. Perez, M. D. Cuy, and R. C. Robinson, ‘Mach 0.3 Burner Rig Facility at the NASA Glenn Materials Research Laboratory’, E-17628, Mar. 2011.
[183] R. Vaßen et al., ‘Recent Activities in the Field of Thermal Barrier Coatings Including Burner Rig Testing in the European Union’, Advanced Engineering Materials, vol. 10, no. 10, Art. no. 10, Oct. 2008, doi: 10.1002/adem.200800015.
[184] V. Maurel et al., ‘Recent Progress in Local Characterization of Damage Evolution in Thermal Barrier Coating Under Thermal Cycling’, in Superalloys 2020, S. Tin, M. Hardy, J. Clews, J. Cormier, Q. Feng, J. Marcin, C. O’Brien, and A. Suzuki, Eds., in The Minerals, Metals & Materials Series. Cham: Springer International Publishing, 2020, pp. 813–823. doi: 10.1007/978-3-030-51834-9_80.
[185] D. R. Mumm, M. Watanabe, A. G. Evans, and J. A. Pfaendtner, ‘The influence of test method on failure mechanisms and durability of a thermal barrier system’, Acta Materialia, vol. 52, no. 5, pp. 1123–1131, Mar. 2004, doi: 10.1016/j.actamat.2003.10.045.
[186] J. I. Eldridge, C. M. Spuckler, K. W. Street, and J. R. Markham, ‘Infrared Radiative Properties of Yttria–Stabilized Zirconia Thermal Barrier Coatings’, in 26th Annual Conference on Composites, Advanced Ceramics, Materials, and Structures: Ceramic Engineering and Science Proceedings, John Wiley & Sons, Ltd, 2002, pp. 417–430.
[187] J. T. Demasi and M. Ortiz, ‘Thermal barrier coating life prediction model development, phase 1’, NASA-CR-182230, Dec. 1989. Accessed: Sep. 15, 2022. [Online]. Available: https://ntrs.nasa.gov/citations/19900004072
[188] C. C. Berndt et al., ‘Current problems in plasma spray processing’, JTST, vol. 1, no. 4, pp. 341–356, Dec. 1992, doi: 10.1007/BF02647162.
[189] M. Shinozaki, K. A. Roberts, B. van de Goor, and T. W. Clyne, ‘Deposition of Ingested Volcanic Ash on Surfaces in the Turbine of a Small Jet Engine’, Advanced Engineering Materials, vol. 15, no. 10, pp. 986–994, 2013, doi: 10.1002/adem.201200357.
[190] D. S. Fox et al., ‘Natural Gas/Oxygen Burner Rig at The NASA Glenn Materials Research Laboratory’, E-20020, Mar. 2022.
[191] E. Gildersleeve, V. Viswanathan, and S. Sampath, ‘Molten silicate interactions with plasma sprayed thermal barrier coatings: Role of materials and microstructure’, Journal of the European Ceramic Society, vol. 39, no. 6, pp. 2122–2131, Jun. 2019, doi: 10.1016/j.jeurceramsoc.2019.01.023.
[192] D. E. Mack, T. Wobst, M. O. D. Jarligo, D. Sebold, and R. Vaßen, ‘Lifetime and failure modes of plasma sprayed thermal barrier coatings in thermal gradient rig tests with simultaneous CMAS injection’, Surface and Coatings Technology, vol. 324, pp. 36–47, Sep. 2017, doi: 10.1016/j.surfcoat.2017.04.071.
[193] F. Mauget, F. Hamon, M. Morisset, J. Cormier, F. Riallant, and J. Mendez, ‘Damage mechanisms in an EB-PVD thermal barrier coating system during TMF and TGMF testing conditions under combustion environment’, International Journal of Fatigue, vol. 99, pp. 225–234, Jun. 2017, doi: 10.1016/j.ijfatigue.2016.08.001.
[194] L. Despres, ‘Comportement en fatigue thermomécanique à haute température d’un système barrière thermique texturé par laser’, Université Bourgogne Franche-Comté, 2020.

[195] T. Wang et al., ‘Corrosion behavior of air plasma spraying zirconia-based thermal barrier coatings subject to Calcium–Magnesium–Aluminum-Silicate (CMAS) via burner rig test’, Ceramics International, vol. 46, no. 11, Part B, pp. 18698–18706, Aug. 2020, doi: 10.1016/j.ceramint.2020.04.184.
[196] P. Jana, P. S. Jayan, S. Mandal, and K. Biswas, ‘Thermal cycling life and failure analysis of rare earth magnesium hexaaluminate based advanced thermal barrier coatings at 1400°C’, Surface and Coatings Technology, vol. 328, pp. 398–409, Nov. 2017, doi: 10.1016/j.surfcoat.2017.09.019.
[197] R. Naraparaju et al., ‘Integrated testing approach using a customized micro turbine for a volcanic ash and CMAS related degradation study of thermal barrier coatings’, Surface and Coatings Technology, vol. 337, pp. 198–208, Mar. 2018, doi: 10.1016/j.surfcoat.2018.01.030.
[198] R. Vaßen et al., ‘Performance of YSZ and Gd2Zr2O7/YSZ double layer thermal barrier coatings in burner rig tests’, Journal of the European Ceramic Society, vol. 40, no. 2, pp. 480–490, Feb. 2020, doi: 10.1016/j.jeurceramsoc.2019.10.021.
[199] Robert Vaßen, ‘Entwicklung neuer oxidischer Wärmedämmschichten für Anwendungen in stationären und Flug-Gasturbinen’, Forschungszentrum Jülich GmbH, 2004.
[200] J. M. Drexler, A. Aygun, D. Li, R. Vaßen, T. Steinke, and N. P. Padture, ‘Thermal-gradient testing of thermal barrier coatings under simultaneous attack by molten glassy deposits and its mitigation’, Surface and Coatings Technology, vol. 204, no. 16, pp. 2683–2688, May 2010, doi: 10.1016/j.surfcoat.2010.02.026.
[201] N. Kumar, S. Mahade, A. Ganvir, and S. Joshi, ‘Understanding the influence of microstructure on hot corrosion and erosion behavior of suspension plasma sprayed thermal barrier coatings’, Surface and Coatings Technology, vol. 419, p. 127306, Aug. 2021, doi: 10.1016/j.surfcoat.2021.127306.
[202] S. Mahade, ‘Functional Performance of Gadolinium Zirconate/Yttria Stabilized Zirconia Multi-Layered Thermal Barrier Coatings’, 2018.
[203] C. G. Levi, ‘Emerging materials and processes for thermal barrier systems’, Current Opinion in Solid State and Materials Science, vol. 8, no. 1, Art. no. 1, Jan. 2004, doi: 10.1016/j.cossms.2004.03.009.
[204] G. Mauer, M. O. Jarligo, D. E. Mack, and R. Vaßen, ‘Plasma-Sprayed Thermal Barrier Coatings: New Materials, Processing Issues, and Solutions’, Journal of Thermal Spray Technology, vol. 22, no. 5, Art. no. 5, Jun. 2013, doi: 10.1007/s11666-013-9889-8.
[205] R. Vaßen, M. O. Jarligo, T. Steinke, D. E. Mack, and D. Stöver, ‘Overview on advanced thermal barrier coatings’, Surface and Coatings Technology, vol. 205, no. 4, pp. 938–942, Nov. 2010, doi: 10.1016/j.surfcoat.2010.08.151.
[206] M. R. Winter and D. R. Clarke, ‘Oxide Materials with Low Thermal Conductivity’, Journal of the American Ceramic Society, vol. 90, no. 2, Art. no. 2, 2007, doi: 10.1111/j.1551-2916.2006.01410.x.
[207] A. Pragatheeswaran et al., ‘Plasma spray-deposited lanthanum phosphate coatings for protection against molten uranium corrosion’, Surface and Coatings Technology, vol. 265, pp. 166–173, Mar. 2015, doi: 10.1016/j.surfcoat.2015.01.040.
[208] R. Vaßen, E. Bakan, D. E. Mack, and O. Guillon, ‘A Perspective on Thermally Sprayed Thermal Barrier Coatings: Current Status and Trends’, J Therm Spray Tech, vol. 31, no. 4, pp. 685–698, Apr. 2022, doi: 10.1007/s11666-022-01330-2.
[209] E. Bakan and R. Vaßen, ‘Ceramic Top Coats of Plasma-Sprayed Thermal Barrier Coatings: Materials, Processes, and Properties’, J Therm Spray Tech, vol. 26, no. 6, Art. no. 6, Aug. 2017, doi: 10.1007/s11666-017-0597-7.
[210] L. Xu, H. Wang, L. Su, D. Lu, K. Peng, and H. Gao, ‘A new class of high-entropy fluorite oxides with tunable expansion coefficients, low thermal conductivity and exceptional sintering resistance’, Journal of the European Ceramic Society, vol. 41, no. 13, pp. 6670–6676, Oct. 2021, doi: 10.1016/j.jeurceramsoc.2021.05.043.
[211] D. Song et al., ‘Glass-like thermal conductivity in mass-disordered high-entropy (Y,Yb)2(Ti, Zr, Hf)2O7 for thermal barrier material’, Materials & Design, vol. 210, p. 110059, Nov. 2021, doi: 10.1016/j.matdes.2021.110059.

[212] D. Zhu, ‘Design and Performance Optimizations of Advanced Erosion-Resistant Low Conductivity Thermal Barrier Coatings for Rotorcraft Engines’, May 2012.
[213] N. Schlegel, D. Sebold, Y. J. Sohn, G. Mauer, and R. Vaßen, ‘Cycling Performance of a Columnar-Structured Complex Perovskite in a Temperature Gradient Test’, Journal of Thermal Spray Technology, vol. 24, no. 7, Art. no. 7, Oct. 2015, doi: 10.1007/s11666-015-0254-y.
[214] D. Zhu, J. A. Nesbitt, T. R. Mccue, C. A. Barrett, and R. A. Miller, ‘Furnace Cyclic Behavior of Plasma–Sprayed Zirconia–Yttria and Multi–Component Rare Earth Oxide Doped Thermal Barrier Coatings’, in 26th Annual Conference on Composites, Advanced Ceramics, Materials, and Structures: B: Ceramic Engineering and Science Proceedings, John Wiley & Sons, Ltd, 2002, pp. 533–545. doi: 10.1002/9780470294758.ch59.
[215] R. Vassen, F. Traeger, and D. Stöver, ‘New Thermal Barrier Coatings Based on Pyrochlore/YSZ Double-Layer Systems’, International Journal of Applied Ceramic Technology, vol. 1, no. 4, pp. 351–361, 2004.
[216] U. Schulz and W. Braue, ‘Degradation of La2Zr2O7 and other novel EB-PVD thermal barrier coatings by CMAS (CaO–MgO–Al2O3–SiO2) and volcanic ash deposits’, Surface and Coatings Technology, vol. 235, pp. 165–173, Nov. 2013, doi: 10.1016/j.surfcoat.2013.07.029.
[217] J. M. Drexler, A. L. Ortiz, and N. P. Padture, ‘Composition effects of thermal barrier coating ceramics on their interaction with molten Ca–Mg–Al–silicate (CMAS) glass’, Acta Materialia, vol. 60, no. 15, pp. 5437–5447, Sep. 2012, doi: 10.1016/j.actamat.2012.06.053.
[218] N. L. Ahlborg and D. Zhu, ‘Calcium–magnesium aluminosilicate (CMAS) reactions and degradation mechanisms of advanced environmental barrier coatings’, Surface and Coatings Technology, vol. 237, pp. 79–87, Dec. 2013, doi: 10.1016/j.surfcoat.2013.08.036.
[219] J. Xia et al., ‘On the resistance of rare earth oxide-doped YSZ to high temperature volcanic ash attack’, Surface and Coatings Technology, vol. 307, pp. 534–541, Dec. 2016, doi: 10.1016/j.surfcoat.2016.09.033.
[220] M. G. Gok and G. Goller, ‘Microstructural characterization of GZ/CYSZ thermal barrier coatings after thermal shock and CMAS+hot corrosion test’, Journal of the European Ceramic Society, Feb. 2017, doi: 10.1016/j.jeurceramsoc.2017.02.004.
[221] A. Nieto et al., ‘Layered, composite, and doped thermal barrier coatings exposed to sand laden flows within a gas turbine engine: Microstructural evolution, mechanical properties, and CMAS deposition’, Surface and Coatings Technology, vol. 349, pp. 1107–1116, Sep. 2018, doi: 10.1016/j.surfcoat.2018.05.089.
[222] P. G. Lashmi et al., ‘Solution combustion synthesis of calcia-magnesia-aluminosilicate powder and its interaction with yttria-stabilized zirconia and co-doped yttria-stabilized zirconia’, Ceramics International, vol. 45, no. 15, Art. no. 15, Oct. 2019, doi: 10.1016/j.ceramint.2019.06.036.
[223] D. L. Poerschke and C. G. Levi, ‘Effects of cation substitution and temperature on the interaction between thermal barrier oxides and molten CMAS’, Journal of the European Ceramic Society, vol. 35, no. 2, pp. 681–691, Feb. 2015, doi: 10.1016/j.jeurceramsoc.2014.09.006.
[224] P. Mechnich and W. Braue, ‘Volcanic Ash-Induced Decomposition of EB-PVD Gd2Zr2O7 Thermal Barrier Coatings to Gd-Oxyapatite, Zircon, and Gd, Fe-Zirconolite’, Journal of the American Ceramic Society, vol. 96, no. 6, pp. 1958–1965, 2013, doi: 10.1111/jace.12251.
[225] R. Kumar, D. Cietek, C. Jiang, J. Roth, M. Gell, and E. H. Jordan, ‘Influence of microstructure on the durability of gadolinium zirconate thermal barrier coatings using APS & SPPS processes’, Surface and Coatings Technology, vol. 337, pp. 117–125, Mar. 2018, doi: 10.1016/j.surfcoat.2018.01.004.
[226] C. G. Levi, ‘Science Underpinning TBC Design for Durability in Aggressive Environments’, DTIC, 2008.
[227] A. Dolmaire et al., ‘Reaction mechanisms of Gd2Zr2O7 in silicate melts derived from CAS’, Journal of the European Ceramic Society, vol. 42, no. 15, pp. 7247–7257, Dec. 2022, doi: 10.1016/j.jeurceramsoc.2022.08.051.
[228] S. Yang, W. Song, Y. Lavallee, X. Zhou, D. B. Dingwell, and H. Guo, ‘Dynamic spreading of re-melted volcanic ash bead on thermal barrier coatings’, Corrosion Science, vol. 170, p. 108659, Jul. 2020, doi: 10.1016/j.corsci.2020.108659.

[229] W. Song and H. Guo, ‘CMAS Dilemma in Jet Engines: Beginning or Ending?’, matlab, pp. 220042–4, Aug. 2022, doi: 10.54227/mlab.20220042.
[230] R. M. Leckie, S. Krämer, M. Rühle, and C. G. Levi, ‘Thermochemical compatibility between alumina and ZrO2–GdO3/2 thermal barrier coatings’, Acta Materialia, vol. 53, no. 11, pp. 3281–3292, Jun. 2005, doi: 10.1016/j.actamat.2005.03.035.
[231] A. U. Munawar, U. Schulz, G. Cerri, and H. Lau, ‘Microstructure and cyclic lifetime of Gd and Dy-containing EB-PVD TBCs deposited as single and double-layer on various bond coats’, Surface and Coatings Technology, vol. 245, pp. 92–101, Apr. 2014, doi: 10.1016/j.surfcoat.2014.02.047.
[232] M. P. Schmitt, A. K. Rai, R. Bhattacharya, D. Zhu, and D. E. Wolfe, ‘“Multilayer thermal barrier coating (TBC) architectures utilizing rare earth doped YSZ and rare earth pyrochlores”’, Surface and Coatings Technology, vol. 251, pp. 56–63, Jul. 2014, doi: 10.1016/j.surfcoat.2014.03.049.
[233] S. Mahade, N. Curry, S. Björklund, N. Markocsan, P. Nylén, and R. Vaßen, ‘Erosion Performance of Gadolinium Zirconate-Based Thermal Barrier Coatings Processed by Suspension Plasma Spray’, Journal of Thermal Spray Technology, vol. 26, no. 1–2, pp. 108–115, Jan. 2017, doi: 10.1007/s11666-016-0479-4.
[234] S. Mahade, N. Curry, S. Björklund, N. Markocsan, P. Nylén, and R. Vaßen, ‘Functional performance of Gd2Zr2O7/YSZ multi-layered thermal barrier coatings deposited by suspension plasma spray’, Surface and Coatings Technology, Dec. 2016, doi: 10.1016/j.surfcoat.2016.12.062.
[235] S. Mahade, N. Curry, K. P. Jonnalagadda, R. L. Peng, N. Markocsan, and P. Nylén, ‘Influence of YSZ layer thickness on the durability of gadolinium zirconate/YSZ double-layered thermal barrier coatings produced by suspension plasma spray’, Surface and Coatings Technology, vol. 357, pp. 456–465, Jan. 2019, doi: 10.1016/j.surfcoat.2018.10.046.
[236] S. Morelli, S. Bursich, V. Testa, G. Bolelli, A. Miccichè, and L. Lusvarghi, ‘CMAS corrosion and thermal cycling fatigue resistance of alternative thermal barrier coating materials and architectures: A comparative evaluation’, Surface and Coatings Technology, vol. 439, p. 128433, Jun. 2022, doi: 10.1016/j.surfcoat.2022.128433.
[237] D. Zhou et al., ‘Thermal cycling performances of multilayered yttria-stabilized zirconia/gadolinium zirconate thermal barrier coatings’, Journal of the American Ceramic Society, vol. 103, no. 3, pp. 2048–2061, 2020, doi: 10.1111/jace.16862.
[238] W. C. Hasz, M. P. Borom, and C. A. Johnson, ‘Protected thermal barrier coating composite with multiple coatings’, US6261643B1, Jul. 17, 2001 Accessed: Jun. 26, 2018. [Online]. Available: https://patents.google.com/patent/US6261643B1/en
[239] L. Bianchi, A. Joulia, and B. D. R. J. Bernard, ‘Revetement anti-cmas a efficacite renforcee’, FR3067391A1, Dec. 14, 2018 Accessed: Jan. 12, 2020. [Online]. Available: https://patents.google.com/patent/FR3067391A1/en?q=non-wetting&q=CMAS&q=thermal&q=barrier&q=coatings&oq=non-wetting+CMAS+thermal+barrier+coatings
[240] S. Lokachari et al., ‘Novel thermal barrier coatings with hexagonal boron nitride additives resistant to molten volcanic ash wetting’, Corrosion Science, vol. 168, p. 108587, May 2020, doi: 10.1016/j.corsci.2020.108587.
[241] Y. X. Kang et al., ‘High temperature wettability between CMAS and YSZ coating with tailored surface microstructures’, Materials Letters, vol. 229, pp. 40–43, Oct. 2018, doi: 10.1016/j.matlet.2018.06.066.
[242] B. Zhang et al., ‘Novel thermal barrier coatings repel and resist molten silicate deposits’, Scripta Materialia, vol. 163, pp. 71–76, Apr. 2019, doi: 10.1016/j.scriptamat.2018.12.028.
[243] S.-J. Yang, W.-J. Song, D. B. Dingwell, J. He, and H.-B. Guo, ‘Surface roughness affects metastable non-wetting behavior of silicate melts on thermal barrier coatings’, Rare Met., vol. 41, no. 2, pp. 469–481, Feb. 2022, doi: 10.1007/s12598-021-01773-6.
[244] W. Song et al., ‘Biomimetic Super “Silicate” Phobicity and Superhydrophobicity of Ceramic Material’, Advanced Materials Interfaces, vol. 9, no. 32, p. 2201267, 2022, doi: 10.1002/admi.202201267.

[245] Y. Wang et al., ‘Preparation and CMAS Wettability Investigation of CMAS Corrosion Resistant Protective Layer with Micro-Nano Double Scale Structure’, Coatings, vol. 12, no. 5, Art. no. 5, May 2022, doi: 10.3390/coatings12050648.
[246] Y. Guo et al., ‘Ultrafast laser reconstructed PS-PVD thermal barrier coatings with superior silicophobic triple-scale micro/nano structure’, Materials & Design, vol. 228, p. 111846, Apr. 2023, doi: 10.1016/j.matdes.2023.111846.
[247] H. Wu, K. Huo, F. Ye, Y. Hua, and F. Dai, ‘Wetting and spreading behavior of molten CMAS on the laser textured thermal barrier coatings with the assistance of Pt-modification’, Applied Surface Science, vol. 622, p. 156887, Jun. 2023, doi: 10.1016/j.apsusc.2023.156887.
[248] W. Qu, S. Li, J. Jing, Y. Pei, and S. Gong, ‘The spreading behavior of CMAS melt on YSZ single crystal with low index orientation’, Applied Surface Science, vol. 527, p. 146846, Oct. 2020, doi: 10.1016/j.apsusc.2020.146846.
[249] F. Huanjie, W. Weize, and Y. U. Zexin, ‘Preparation of Micro-Nano Hierarchical Microstructure and Its Performance against CMAS Wetting of Thermal Barrier Coatings’, HDLGDXXBZRKXB, vol. 48, pp. 1–8, Jun. 2022, doi: 10.14135/j.cnki.1006-3080.20220331001.
[250] D. Ushmaev, A. Norton, and J. Kell, ‘Thermally sprayed coatings resistant to environmental degradation: Columnar-like coatings through laser ablation and surface melting approach’, Surface and Coatings Technology, vol. 460, p. 129394, May 2023, doi: 10.1016/j.surfcoat.2023.129394.
[251] L. Guo, Y. Gao, Y. Cheng, J. Sun, F. Ye, and L. Wang, ‘Microstructure design of the laser glazed layer on thermal barrier coatings and its effect on the CMAS corrosion’, Corrosion Science, vol. 192, p. 109847, Nov. 2021, doi: 10.1016/j.corsci.2021.109847.